

國立臺灣大學理學院物理學系

碩士論文

Department of Physics

College of Science

National Taiwan University

Master Thesis

半導體奈米結構光學性質之研究與應用：

氮化銦鎵/氮化鎵多層量子井與氧化鋅奈米柱

Studies and Applications of Optical Properties in Semiconductor

Nanostructures:

InGaN/GaN multiple quantum wells and ZnO nanorods



施函宇

Han-Yu Shih

指導教授：陳永芳 博士

Advisor: Yang-Fang Chen, Ph.D.

中華民國 97 年 6 月

June, 2008

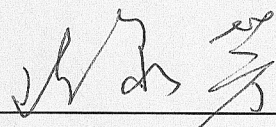
國立臺灣大學 (碩) 博士學位論文
口試委員會審定書

半導體奈米結構光學性質之研究與應用：
氮化銦鎵/氮化鎵多層量子井與氧化鋅奈米柱

Studies and Applications of Optical Properties in
Semiconductor Nanostructures:
InGaN/GaN multiple quantum wells and ZnO nanorods

本論文係 施函宇 君 (學號 R95222063) 在國立臺灣大學物理學系、所完成之碩士學位論文，於民國九十七年六月二十五日承下列考試委員審查通過及口試及格，特此證明

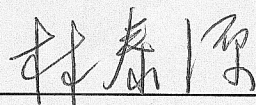
口試委員：



(簽名)

(指導教授)





致謝

猶記得兩年前，懵懂的我踏進全國物理學最高的殿堂，並在學長姊的介紹之下加入了半導體實驗團隊，開始我的碩士生涯。如今在我的研究領域獲得一些成果，乃多虧以下這些人的協助。

首先我要感謝對我幫助最多的兩個人，指導教授陳永芳老師和大師兄陳宗德學長。陳老師在我迷惘的時候指引我研究的方向，在我鬆懈的時候以鼓勵代替責備，並且耐心地指導我完成此篇論文，讓我見識到一位偉大學者的風範。宗德學長傳授我絕大部分的實驗技術，陪我討論實驗數據及改進實驗方法，他學問淵博、待人和善又富責任感，正是我學習的榜樣與目標。再來要感謝林夏玉學姊，我從學姊這邊見識到做研究應有的精神與態度，而實驗室也在學姊的管理下能夠順利運作、井然有序。此外博士班的仲良、瀚葵、群雄、志偉、俊儀、志銘、奕任、世豪、志彬學長們，也在我研究與學業方面給予頗多的建議及協助，這些學長都是我學習與尊敬的對象。

接下來我要感謝熱心提供樣品的實驗助理彥嘉，以及在實驗與課業方面和我一同努力的國裕、威宏、宗玄、中澤、孟霖、振華等碩士班的同學們。多虧你們的陪伴，我的碩士生涯才能如此快樂、充實、多采多姿。

最後，也是最重要的，我要感謝我的家人。當我實驗遭遇挫折而心情低落時，有父母和弟弟的鼓勵與支持；當我研究獲得成果時他們亦開心的和我分享喜悅。而我相信在天堂的祖父、祖母更是樂見我這兩年的進步與成長。

需要被感謝的人太多了，我無法在此一一列舉。但無論如何，我誠心地感激你們在這些日子對我的幫助！

摘要

奈米科技帶給人們極大的便利性與前瞻性，而半導體材料更廣泛地被製作成奈米結構，其展現出與塊材相異甚大的電性、磁性以及光學性質。本論文探討兩種半導體奈米結構的光學特性：氮化銦鎵/氮化鎵多層量子井、氧化鋅奈米柱，並且發現了頗為新奇且有趣之現象。

烏采結構之氮化物通常具備有不錯的壓電效應，因此氮化銦鎵/氮化鎵多層量子井內存在著強烈的內建電場，此特性可被我們應用成為生物感測器。當去氧核醣核酸(DNA)在感測器的表面發生雜合反應，其電偶極改變了氮化銦鎵/氮化鎵多層量子井內的電場，因為量子侷限史塔克效應的關係，量子井的光致螢光光譜、拉曼散射光譜以及我們估算出的氮化銦鎵晶格應變量也會有所變化，此結果代表氮化銦鎵/氮化鎵多層量子井可被開發成為DNA定序晶片之廣大可能性。

另一方面，本團隊已經在去年發現氧化鋅奈米柱內存在著光彈性效應，而我們更預測在越細的氧化鋅奈米柱內，其光彈性效應越明顯。此論文內探測了粗、中、細三種不同直徑的氧化鋅奈米柱之光致螢光光譜、拉曼散射光譜以及估算的晶格應變量隨著激發光源強度的不同，而有所變化。其中以細的氧化鋅奈米柱變化量最為可觀，不但驗證了我們的論點，並貢獻了新穎的資訊給光電元件開發者。

關鍵詞：

奈米科技、去氧核醣核酸雜合、量子井、氧化鋅奈米柱、光彈性效應。

Abstract

Nanotechnology gives people a great future and conveniences. Semiconductor materials are widely made into nanostructures, and they show rather different electrical, magnetic, and optical properties from bulk materials. In this thesis, we investigated two semiconductor nanostructures, InGaN/GaN multiple quantum wells (MQWs) and ZnO nanorods, and found some novel phenomena.

There usually exists a good piezoelectric effect in nitride wurtzite structure, such that InGaN/GaN MQWs have obvious build-in electric field in them, and this property could be used to construct a biosensor. As the hybridization process of deoxyribonucleic acid (DNA) occurs on InGaN/GaN MQWs, the electric field in MQWs would be altered by the polarity of DNA molecules, and the photoluminescence (PL) spectra, Raman spectra, and the calculated strain of InGaN lattice could also be changed due to the quantum confined Stark effect. As a result, InGaN/GaN MQWs have a great opportunity in the development of DNA-sequence identification.

On the other hand, our group had found a phenomenon called photoelastic effect in ZnO nanorods last year, and we further expected that the thinner nanorods, the mightier photoelastic effect exists in them. In this thesis, three diameters of thick, mid-thick, and thin ZnO nanorods are studied. It was observed that the PL spectra, Raman spectra, and

the calculated strain would be changed with different excitation Laser power. Besides, the amounts of change are greater in thinner nanorods. This result gives a good evidence to proof our expectation, and provides much novel information to optoelectric device developers.

Key Words:

nanotechnology, DNA hybridization, quantum well, ZnO nanorod, photoelastic effect.



Contents

致謝.....	I
摘要.....	II
Abstract	III
Contents	V
Figure Caption	VII
1. Introduction	1
2. Theoretical Background	6
2.1 Growth Methods of Samples.....	7
2.1.1 Metal-organic Vapor Phase Epitaxy.....	7
2.1.2 Vapor-Liquid-Solid Growth.....	10
2.1.3 DC Sputter Deposition.....	13
2.2 Fermi Energy.....	14
2.2.1 Fermi Energy for Semiconductor.....	15
2.2.2 Work Function and Fermi Energy for Metal.....	17
2.3 Photoluminescence.....	18
2.4 Raman Scattering.....	23
2.5 Properties of Deoxyribonucleic Acid (DNA).....	29
2.6 Scanning Electron Microscopy.....	35

3. Optical Detection of Deoxyribonucleic Acid Hybridization with InGaN/GaN Multiple Quantum Wells.....	43
3.1 Introduction.....	44
3.2 Experiment.....	46
3.3 Results and Discussion.....	48
3.4 Conclusion.....	55
4. Size-dependent Photoelastic Effect in ZnO Nanorods.....	58
4.1 Introduction.....	59
4.2 Experiment.....	60
4.3 Results and Discussion.....	61
4.4 Conclusion.....	71
5. Summary.....	75



Figure Caption

Fig. 2.1	A schematic illustration in metal-organic vapor phase deposition.	8
Fig. 2.2	A schematic illustration of the apparatus of MOVPE.	9
Fig. 2.3	The illustration of Vapour-Liquid-Solid growth process.	12
Fig. 2.4	A schematic illustration of the apparatus of DC sputtering deposition.	14
Fig. 2.5	The energy diagram of Fermi level, where E_{gap} is the energy gap of semiconductor, $f(E)$ is Fermi-Dirac distribution function.	16
Fig. 2.6	The energy bands for doped semiconductors. Here, the different types of N-Type and P-Type are attributed the different doped material.	16
Fig. 2.7	A relation illustration about the Work function, Vacuum level, and Fermi level.	17
Fig. 2.8	Energy transitions in (a) direct and (b) indirect gap semiconductors between initial states E_i and final states E_f . For indirect transitions (b) the participation of a phonon (E_{ph}) is required.	19
Fig. 2.9	Schematic diagram of radiative transitions between the conduction band (E_C), the valence band (E_V) and exciton (E_X), donor (E_D) and acceptor (E_A) levels in a semiconductor.	21
Fig. 2.10	This spectrum showing the photoluminescence peak and the Raman phonon mode of a CdMnTe film on a GaAs substrate (Perkowitz, 1991).	24
Fig. 2.11	The diagram shows the conservation rules in the Raman scattering.	26
Fig. 2.12	The Raman spectrum of CCl_4 .	26
Fig. 2.13	A simplified Raman spectroscopy experiment setup with a charged-coupled device (CCD) as the detector.	23

Fig. 2.14	The chemical structure of DNA. Hydrogen bonds are shown as dotted lines.	31
Fig. 2.15	The structure of part of a DNA double helix.	33
Fig. 2.16	Summary of the range and spatial resolution of backscattered electrons, secondary electrons, X-rays, and Auger electrons for electrons incident on a solid.	39
Fig. 3.1	Procedure for the construction of a probe chip. We first sputtered a 5-nm-Au layer onto the MQWs substrate, and then probe DNA molecules with thiol were immobilized onto the Au surface. Finally, MCH solution was infected as spacer molecules.	47
Fig. 3.2	(a) PL spectra from InGaN/GaN MQWs sample under different optical excitation densities. The peak shows a blue shift as the excitation power increases due to the spontaneous and piezoelectric polarizations and quantum confined Stark effect. (b) Band structure of InGaN/GaN quantum wells. It shows that the recombination energy of electron-hole pairs is higher in a flater quantum well.	49
Fig. 3.3	PL spectra from the probe chip in target DNA solution with different concentrations. (a) The peak position shifts toward the high energy side as the matched target DNA concentration increases, while (b) the PL spectra of the mismatched target DNA remain the same.	50
Fig. 3.4	The $A_1(\text{LO})$ phonon in Raman scattering spectra from the probe chip in target DNA solution with different concentrations. (a) The phonon energy shows a low-energy shift with the increase of matched target DNA concentration, while (b) the spectra corresponding to the mismatched target DNA do not change.	52
Fig. 3.5	Calculated strain of InGaN/GaN MQWs in the probe chip as a function of target DNA concentration based on Eq. (1). The hybridization process alters the strain of InGaN/GaN MQWs in matched DNA solution, while the MQWs' strain remain unchanged in mismatched DNA solution.	54

Fig. 4.1	Scanning electron microscopy images of ZnO nanorods with different diameters.	62
Fig. 4.2	Photoluminescence spectra of ZnO nanorods with different diameters.	63
Fig. 4.3	Integrated intensity ratio between band-edge and defect emissions as a function of average wire radii, and a fit using Eq. (4.1).	65
Fig. 4.4	Schematic of the band bending of ZnO nanorods under (a) low and (b) high optical excitation power.	66
Fig. 4.5	Excitation-power-dependence of photoluminescence spectra for ZnO nanorods with different diameters. The excitation power increases from the bottom spectrum to top for each set.	67
Fig. 4.6	Excitation-power-dependent Raman scattering spectra of ZnO film and ZnO nanorods with different diameters. The excitation power increases from the bottom spectrum to top for each set.	69
Fig. 4.7	The estimated strength of the biaxial strain as a function of the excitation power for ZnO nanorods for different diameters.	72

Chapter 1

Introduction



Chapter 1 Introduction

Humans have unwittingly employed nanotechnology for thousands of years, for example in making steel, paintings and in vulcanizing rubber.¹ Each of these processes rely on the properties of stochastically-formed atomic ensembles mere nanometers in size, and are distinguished from chemistry in that they do not rely on the properties of individual molecules. But the development of the body of concepts now subsumed under the term nanotechnology has been slower.

The topic of nanotechnology was touched upon by "There's Plenty of Room at the Bottom," a talk given by physicist Richard Feynman at an American Physical Society meeting at Caltech on December 29, 1959. Feynman described a process by which the ability to manipulate individual atoms and molecules might be developed, using one set of precise tools to build and operate another proportionally smaller set, so on down to the needed scale. In the course of this, he noted, scaling issues would arise from the changing magnitude of various physical phenomena: gravity would become less important, surface tension and Van der Waals attraction would become more important, etc. This basic idea appears feasible, and exponential assembly enhances it with parallelism to produce a useful quantity of end products. At the meeting, Feynman announced two challenges, and he offered a prize \$1000 for the first individuals to solve each one. The first challenge involved the construction of a nanomotor, which, to

Feynman's surprise, was achieved by November of 1960 by William McLellan. The second challenge involved the possibility of scaling down letters small enough so as to be able to fit the entire *Encyclopedia Britannica* on the head of a pin; this prize was claimed in 1985 by Tom Newman.²

Nowadays, Nanotechnology is a highly multidisciplinary field, drawing from fields such as applied physics, materials science, interface and colloid science, device physics, supramolecular chemistry (which refers to the area of chemistry that focuses on the noncovalent bonding interactions of molecules), self-replicating machines and robotics, chemical engineering, mechanical engineering, biological engineering, and electrical engineering. Grouping of the sciences under the umbrella of "nanotechnology" has been questioned on the basis that there is little actual boundary-crossing between the sciences that operate on the nano-scale. Instrumentation is the only area of technology common to all disciplines; on the contrary, for example pharmaceutical and semiconductor industries do not "talk with each other". Corporations that call their products "nanotechnology" typically market them only to a certain industrial cluster.³

Examples of nanotechnology are the manufacture of polymers based on molecular structure, and the design of computer chip layouts based on surface science. Despite the promise of nanotechnologies such as quantum dots and nanotubes, real commercial applications have mainly used the advantages of colloidal nanoparticles in bulk form,

such as sunscreen lotion, cosmetics, protective coatings, drug delivery,⁴ and stain resistant clothing.

In this thesis, we demonstrated two sets of study in nanotechnology based on semiconductor-composite nanostructures. First, we develop a biosensor, which could be used for detecting deoxyribonucleic acid (DNA) hybridization, with InGaN/GaN multiple quantum wells (MQWs) as a underlying substrate. The biosensor shows a good performance and should have a great potential in the DNA-sequence identification. Further more, another topic of nanostructure has studied, and a novel phenomenon was observed. In ZnO nanorods, there exists a photoelastic effect which has reported by our group-mates and attracted great attentions recently. Based on that result, size-dependent photoelastic effect was expected due to the difference between thinner nanorods and thicker nanorods. Indeed, the size-dependent photoelastic effect in ZnO nanorods had been observed in this work. In view of the two sets of study, our results could provide helpful contributions in nanotechnology as well as optoelectric devices fabrication methods.

Reference

1. Visakhapatnam, *Indian craftsmen, artisans used nanotech 2000 years ago*,
DECCAN HERALD.
2. Gribbin John, *Richard Feynman: A Life in Science*, Dutton, 1997.
3. Martin Meyer, WHAT DO WE KNOW ABOUT INNOVATION IN
NANOTECHNOLOGY, Helsinki University of Technology, 2006.
4. Abdelwahed W, Degobert G, Stainmesse S, and Fessi H, *Advanced Drug Delivery
Reviews*. **58** (15): 1688-1713 (2006).



Chapter 2

Theoretical Background



Chapter 2 Theoretical Background

2.1 Growth Methods of Samples

2.1.1 Metal-organic Vapour Phase Epitaxy

Metal-organic vapour phase epitaxy (MOVPE) is a chemical vapour deposition method of epitaxial growth of materials, especially compound semiconductors from the surface reaction of organic compounds or metalorganics and metal hydrides containing the required chemical elements. For example, indium phosphide could be grown in a reactor on a substrate by introducing Trimethylindium ((CH₃)₃In) and phosphine (PH₃).¹ Alternative names for this process include organometallic vapour phase epitaxy (OMVPE), metalorganic chemical vapour deposition (MOCVD) and organometallic chemical vapour deposition (OMCVD). Formation of the epitaxial layer occurs by final pyrolysis of the constituent chemicals at the substrate surface as shown in Fig 2.1. In contrast to molecular beam epitaxy (MBE) the growth of crystals is by chemical reaction and not physical deposition. This takes place not in a vacuum, but from the gas phase at moderate pressures (2 to 100 kPa). As such this technique is preferred for the formation of devices incorporating thermodynamically metastable alloys. It has become the dominant process for the manufacture of laser diodes, solar cells, and LEDs.

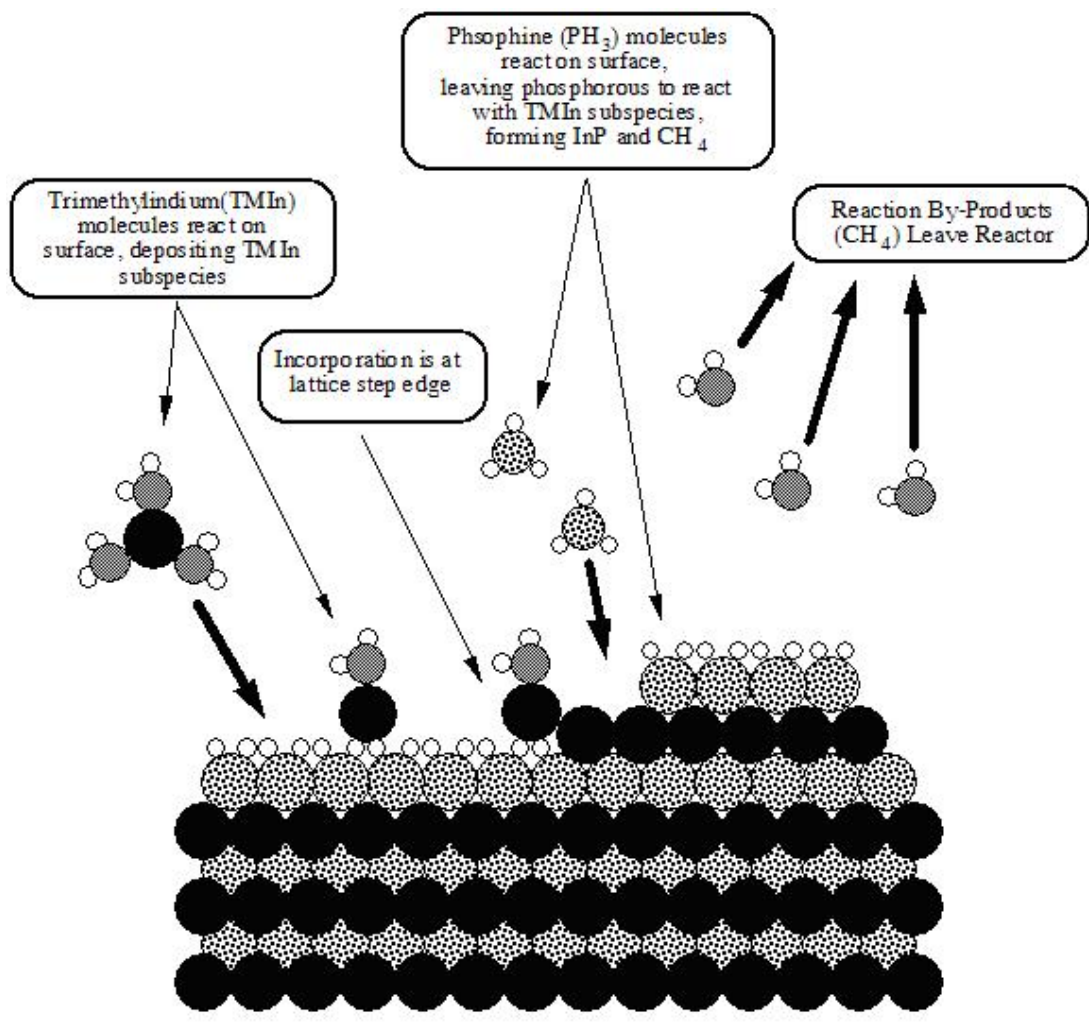


Fig. 2.1

A schematic illustration in metal-organic vapor phase deposition.

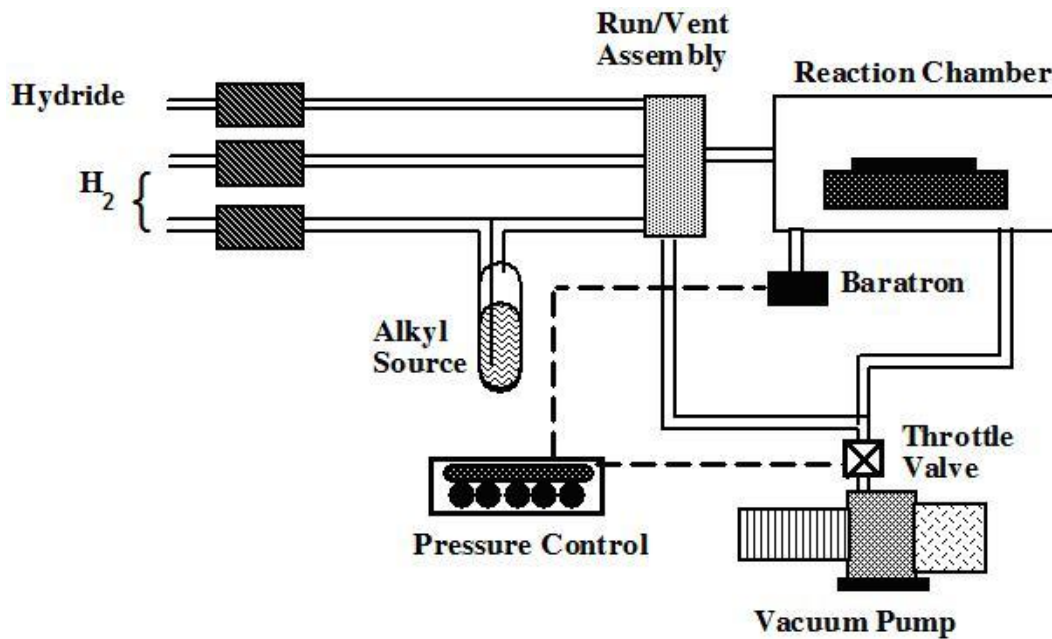


Fig. 2.2
A schematic illustration of the apparatus of MOVPE.

Figure 2.2 shows the apparatus of MOVPE, and we describe four major parts in it as follows:

- **Reactor:** A reactor is a chamber made of a material that does not react with the chemicals being used. It must also withstand high temperatures. This chamber is composed by reactor walls, liner, a susceptor, gas injection units, and temperature control units. Usually, the reactor walls are made from stainless steel or quartz. To prevent over heating, cooling water must be flowing through the channels within the reactor walls. Special glasses, such as quartz or ceramic, are often used as the liner in the reactor chamber between the reactor wall and the susceptor. A substrate sits on a *susceptor* which is at a controlled temperature. The susceptor is made from a material

resistant to the metalorganic compounds used; graphite is sometimes used. For growing nitrides and related materials, a special coating on the graphite susceptor is necessary to prevent corrosion by ammonia (NH_3) gas.

- **Gas inlet and switching system:** Gas is introduced via devices known as 'bubblers'.

In a bubbler a carrier gas (usually nitrogen or hydrogen) is bubbled through the metalorganic liquid, which picks up some metalorganic vapour and transports it to the reactor. The amount of metalorganic vapour transported depends on the rate of carrier gas flow and the bubbler temperature. Allowance must be made for saturated vapours.

- **Pressure maintenance system:** Since the deposition process has to occur in constantly vacuum environment, the pump should work to exhaust nearly all gas to maintain at the necessary pressure.

- **Gas Exhaust and cleaning System:** Toxic waste products must be converted to liquid or solid wastes for recycling (preferably) or disposal. Ideally processes will be designed to minimize the production of waste products.

2.1.2 Vapor -Liquid-Solid Growth

Vapor-liquid-solid (VLS) growth, as an effective route to fabricate semiconductor nanowires (NWs), has been extensively used since it was proposed by Wagner and Ellis in 1964.² The main features of VLS growth are that semiconductor NWs have metal or

alloy droplets on their tips and these droplets (as catalysts) define their diameters and direct their growth orientation. To date, many studies have focused on controlled diameter of semiconductor NWs using the VLS mechanism, as well as thermodynamic and kinetic size limit of NWs' growth. However, few studies of semiconductor NWs growth kinetics are performed, especially theoretical studies.

Therefore, the purpose of this work is to present the effects of semiconductor NWs' size on its growth kinetics by the VLS mechanism and to give the dependences of growth rate and activation energy of crystallization on size quantitatively. Furthermore, the validity of these theoretical results is examined in the case of silicon NWs (SiNWs) growth. These theoretical predictions are in good agreement with the experimental cases.

The typical VLS growth process is shown schematically in Fig 2.3. Generally, VLS growth can be divided by three main steps:

- (1) Metal Catalyst: A thin metal film is deposited on the substrate and annealed to form nanoclusters.
- (2) Vapor-Liquid Process: During growth, the gas precursor carrying source atoms is catalyzed by the liquid metal-semiconductor nanoclusters (the tips of nanowires), and the source atoms are melted into the nanoclusters.
- (3) Liquid-Solid Process: Once the liquid is supersaturated with source atoms, the

precipitation happens at the bottom of liquid (the liquid-solid interface), thus pushing the wire growth and also keeping the catalyst on the top of wires.

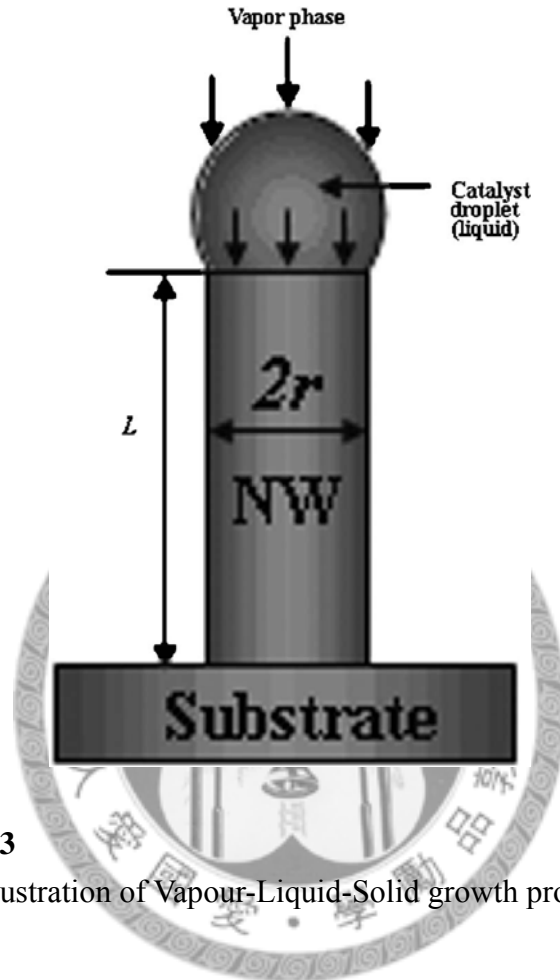


Fig. 2.3
The illustration of Vapour-Liquid-Solid growth process.

For a steady VLS growth process, NW growth species in the liquid droplet should remain in balance, i.e., the number of atoms transferred from the vapor phase to the droplet per unit time is equal to that transformed from liquid to the crystal phase.

The nanowires have several sidewall facets and the number of sidewalls decreases with increasing growth temperature. Growth can happen at both the tip and sidewall, which might widen the nanowires; however, the sidewall growth is not catalyzed, thus the rate is much slower than the tip.

2.1.3 DC Sputter Deposition

Early days, the method of sputter deposition was used to deposit the thin film, or applying the metal in the fabric. When the vacuum technology matures, the sputtering is largely replaced by the evaporation, due to the rate of latter is faster than the former. However, many materials are unable to evaporate by heating the resistance, so this method is still extensively used to produce the composite. A sputtering system (JFC-1600, JEOL) is used in this work. As shown in Fig. 2.4, during sputtering, the substrate is placed in a vacuum chamber with a target of the material to be deposited. The plasma is generated in a passive source gas (i.e. Argon or air) in the chamber and the ion bombardment is directed towards the target, causing material to be sputtered off the target and condense on the chamber walls and the substrate. A strong magnetic field (magnetron) can be used to concentrate the plasma near the target to increase the deposition rate.³

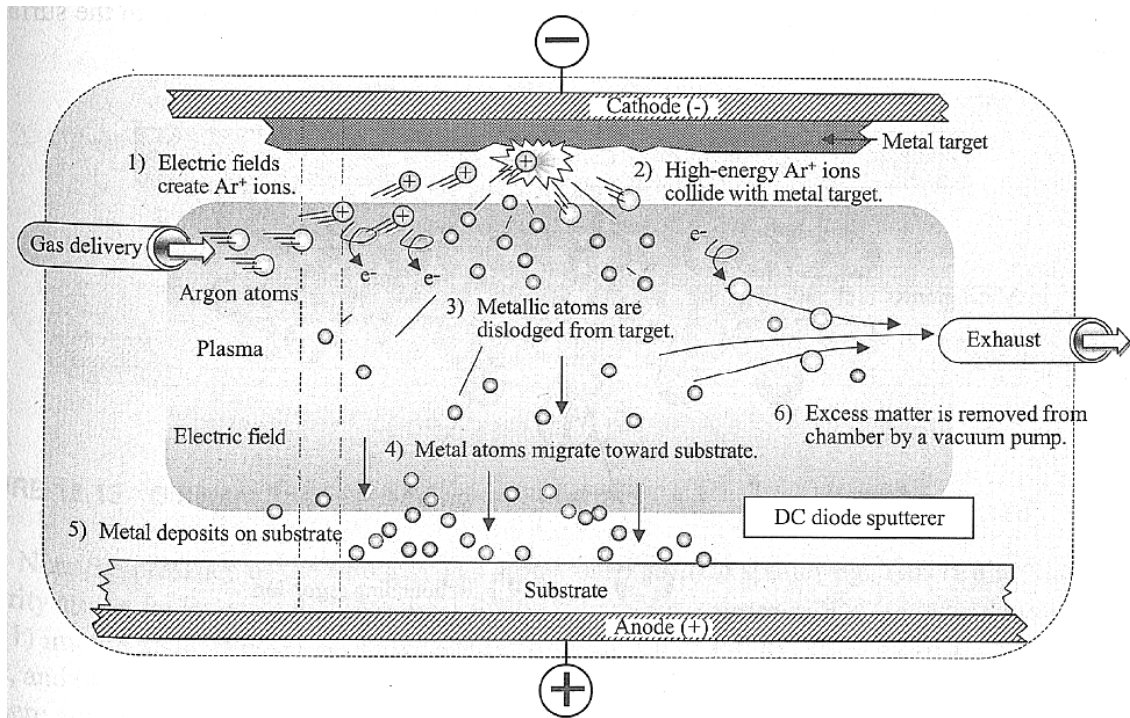


Fig.2.4
A schematic illustration of the apparatus of DC sputtering deposition.

2.2 Fermi Energy

In physics, some particles (for example electrons) follow the Pauli Exclusion Principle: no two particles may occupy the same state at the same time. When a number of electrons are put into a system, electrons will occupy higher energy levels when the lower ones are filled up. By the Pauli Exclusion Principle, we know that the electrons will fill all available energy levels, and the top of that "Fermi sea" of electrons is called the Fermi energy or Fermi level. Loosely speaking, the "Fermi energy" is the energy of the highest occupied state at absolute zero temperature. It is also equivalent to the chemical potential of the system in the ground state at absolute zero. Fermi energy was

named after Enrico Fermi who, with Paul Dirac, derived the Fermi-Dirac statistics. These statistics allow one to predict the behavior of large numbers of electrons under certain circumstances, especially in solids. The concept of the Fermi energy is a crucially important concept for the understanding of the electrical and thermal properties of solids. For instance, Fermi energy is an idea which finds application in semiconductor theory and device design.

2.2.1 Fermi Energy for Semiconductor

To understand the properties of semiconductor, the Fermi energy is the important information. However, the semiconductors can be differentiated between the intrinsic and extrinsic semiconductor. The Fermi energy of the two is all dependent on the temperature and carrier concentration. In intrinsic semiconductor case, the Fermi energy is located at the middle of band gap at absolute zero temperature. In extrinsic semiconductor case, in addition to the temperature, that the impurity (or the doped material) changing the carrier concentration is also a factor to influence the Fermi energy. The simply band diagram of Fermi energy in the general semiconductor and different types is shown in Fig. 2.5 and Fig. 2.6.

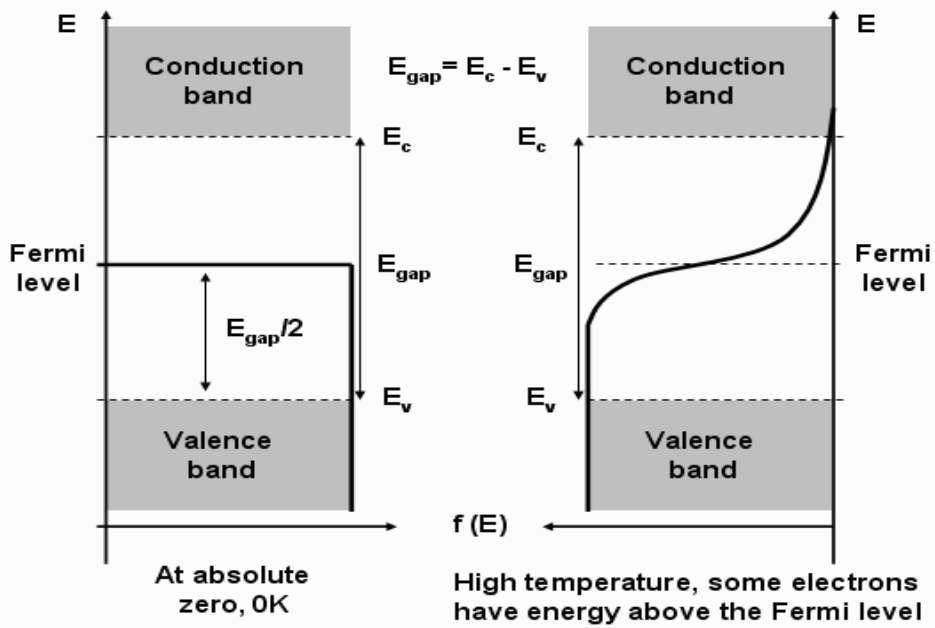


Fig. 2.5

The energy diagram of Fermi level, where E_{gap} is the energy gap of semiconductor, $f(E)$ is Fermi-Dirac distribution function.

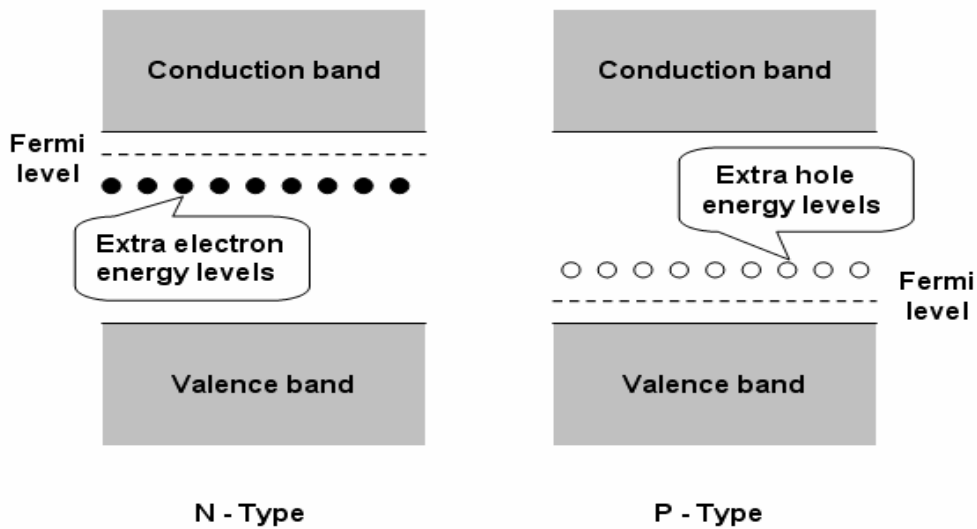


Fig. 2.6

The energy bands for doped semiconductors. Here, the different types of N-Type and P-Type are attributed the different doped material.

2.2.2 Work Function and Fermi Energy for Metal

Work function (W) is the minimum amount of energy needed to remove an electron from the surface of the metal, to a point just outside the metal where the electron has zero kinetic energy. Work function is usually measured in electron-volts (eV). The energy of the most energetic electron in a conductor at absolute zero temperature is known as the Fermi energy (E_F), so the Work function of the metal may also be defined as the minimum energy required to remove the an electron from the Fermi level to a position known as the “ Vacuum level ”. The Vacuum level is the energy of a free electron (zero kinetic energy) in vacuum. Therefore, the Work function can be affected by the changed condition of the surface of a conductor material, such as with the addition or removal of layers on the surface, surface charging oxidation, contamination, and the like. A simply illustration is shown in Fig. 2.7.

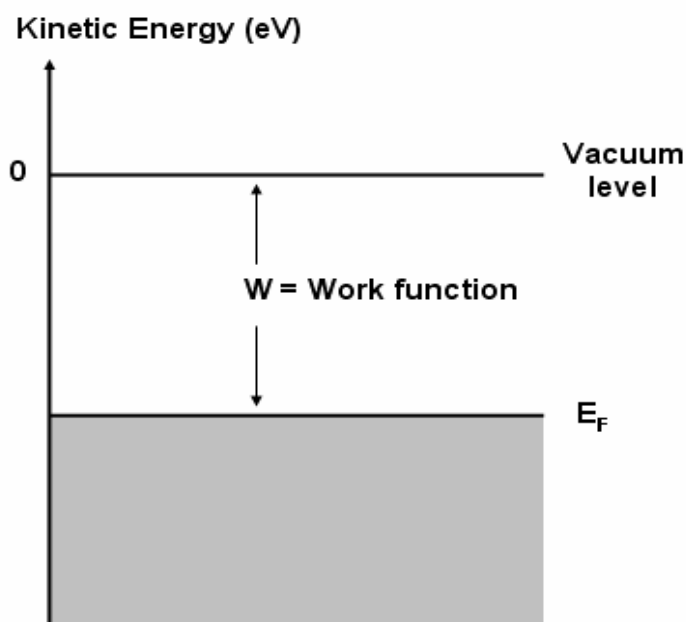


Fig. 2.7

A relation illustration about the Work function, Vacuum level, and Fermi level.

2.3 Photoluminescence

A light source with photon energy higher than the band gap of the semiconductor crystal will excite the carriers to their excited states. As soon as the excitation occurs, all excited electrons and holes will relax to the bottom of the conduction band and the top of valence band, respectively, and then the recombination occurs. Energy and momentum must be conserved during the electronic transitions. When the maximum of the valence band and the conduction band occur at the same value of the wave vector \mathbf{k} [Fig. 2.8], transitions are direct and the material is a direct-gap semiconductor (for example, ZnSe, InP, GaAs). In materials with a direct gap, the most likely transitions are across the minimum energy gap, between the most probably filled states at the minimum of the conduction band, and the states most likely to be unoccupied at the maximum of the valence band. If the band extreme do not occur at the same wave vector \mathbf{k} , transitions are indirect. To conserve momentum in such an indirect-gap material (for example, Si, Ge), phonon participation is required. Thus, the recombination of electron-hole pairs must accompanied by the simultaneous emission of a photon and a phonon. The probability of such a process is significantly lower as compared with direct transitions. The radiative recombination that is difference to the incandescence coming from hot source is called photoluminescence (PL). If there is a multiplicity of excited states, only transitions from the lowest excited state can generally

be observed at low temperature because of rapid thermalization.⁴

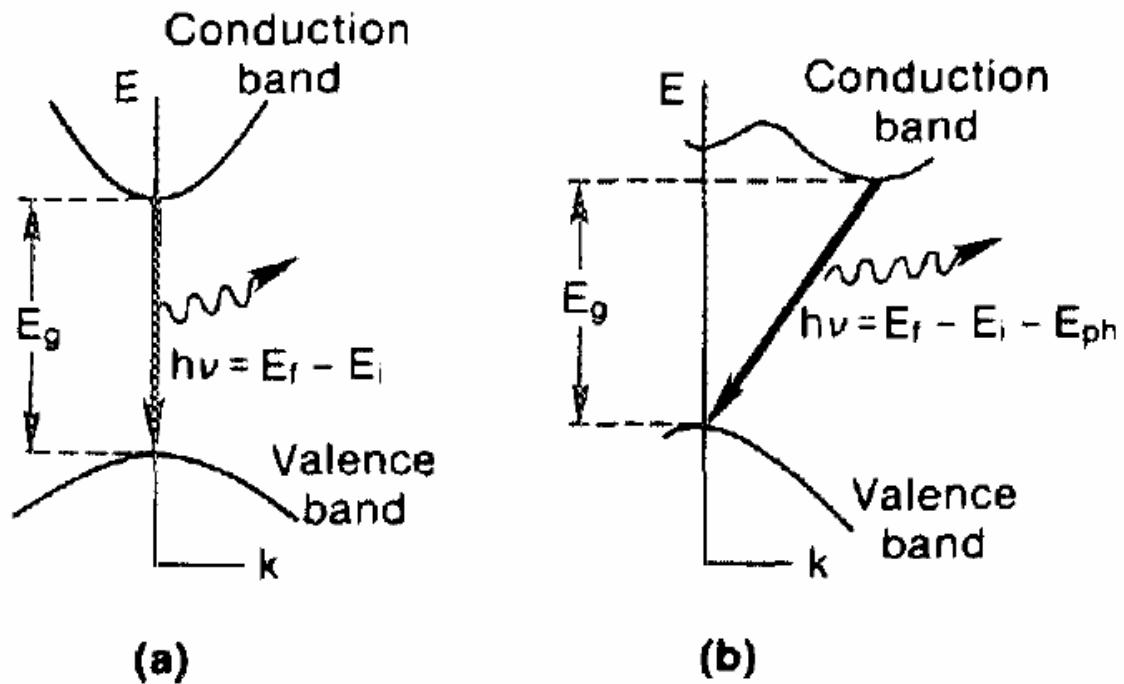


Fig. 2.8

Energy transitions in (a) direct and (b) indirect gap semiconductors between initial states E_i and final states E_f . For indirect transitions (b) the participation of a phonon (E_{ph}) is required.

Photoluminescence is one of the most useful optical methods for the semiconductor industry,^{4,5} with its powerful and sensitive ability to find impurities and defect levels, which affect material's quality and device performance. A given impurity produces a set of characteristic spectral features. This fingerprint identifies the impurity type, and often several different impurities can be seen in a single PL spectrum. In some cases PL goes beyond bare identification, to measure impurity concentrations. In

another use, the half widths of PL peaks are an indication of sample quality and crystallinity, although such analysis has not yet become highly quantitative. Finally, PL is sensitive to stress, and can measure its magnitude and direction. Photoluminescence can also determine semiconductor band gaps. This is important mixed crystals whose gap varies with the compositional parameter x , yet must accurately known for applications. When the relation between gap energy and x is known, the PL measurement of gap can be inverted to determine x .

A simplified set of radiative transitions that lead to emission in semiconductors is giving in Fig. 2.9.

Process 1 is an intraband transition: an electron is excited by a photon well above the conduction band edge dribbles down and reaches thermal equilibrium with the lattice. This thermalization process may lead to phonon-assisted photon emission or, more likely, phonon emission only.

Process 2 is an interband transition: this produce intrinsic luminescence. In this case, direct recombination between an electron in the conduction band and a hole in the valence band results in the emission of a photon of energy $h\nu=E_g$. Although this recombination occurs from states close to the corresponding band edges, the thermal distribution of carriers in these states will lead, in general, to a broad emission spectrum.

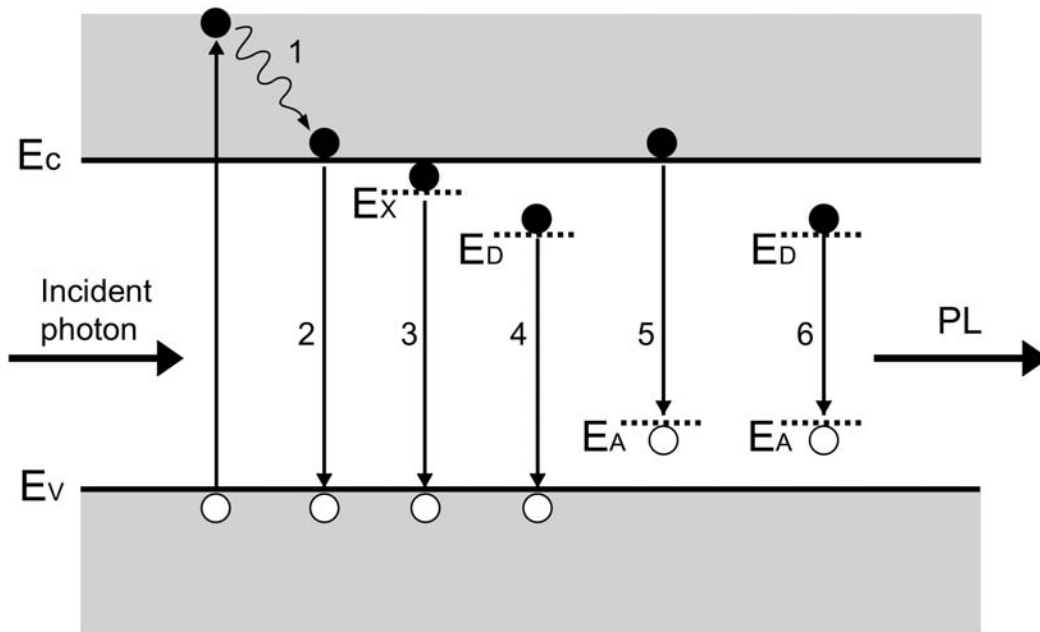


Fig. 2.9

Schematic diagram of radiative transitions between the conduction band (E_C), the valence band (E_V) and exciton (E_X), donor (E_D) and acceptor (E_A) levels in a semiconductor.

Process 3 is the exciton decay observable at low temperature. An exciton is a quasi-particle consisting of a Coulomb-correlated electron-hole pair. The coulombic interaction between this pairs, modified by the dielectric constant of the semiconductor, brings their energy levels closer together than the width of the energy gap. The exciton can wander through the crystal (the electron and the hole are only relatively free because they are associated as a mobile pair). Because of this mobility, the excitation is not a set of spatially localized states.⁶ Excitonic levels are observable at low temperature at which kT is smaller than the excitonic binding energy, which can be

anything from an eV to tenths of an meV depending on the material. The recombination of an exciton will give rise to sharp-line luminescence, with energy of the band gap minus the binding energy of the exciton.

Process 4, 5, and 6 arise from transitions that start and/or finish on localized states of impurities (e.g. donors and acceptors) in the gap: these produce extrinsic luminescence. Process 4 represents the donor-to-free-hole transition as well as process 5 represents the free-electron-to-acceptor transition. Process 6 is the donor-acceptor pair (DAP) recombination. Donor is substitutional atom with a higher number of valence electrons compared with the host atom, whereas acceptor is a substitutional atom with lower of valence electrons. Donor contributes excess electrons to the crystal, while acceptor tends to capture electrons or equivalently donate holes. Donor or acceptor may be electrically charged or neutral.⁷ As the neutral donor and the neutral acceptor are brought closer together, the donor's electron become increasingly shared by the acceptor. In other words, the donor and the acceptor become increasingly more ionized and form a pair.⁶ The energy of the DAP recombination emission in relatively pure crystals can be expressed by:

$$h\nu(r) = E_g - (E_A - E_D) + e^2/\epsilon r \quad (2.1)$$

where E_A and E_D are the binding energies of the acceptor and donor, respectively, ϵ is the dielectric constant, e is the electron charge, and r is the distance between the

donor and acceptor impurities which participate in the recombination. The last term arises from the coulombic interaction of the carriers and depends on the separation r . the radiative transition probability in this case is

$$P(r) = P(0)\exp(-2r/a) \quad (2.2)$$

where a is the Bohr radius of the less tightly bound center, and $P(0)$, the limiting transition probability as $r \rightarrow 0$, is a constant.

It should also be noted that not all recombination between electrons and holes results in light emission, since there may also be efficient nonradiative recombination paths. Examples of nonradiative processes are (1) multi-phonon emission (i.e., direct conversion of the energy of an electron to heat); (2) the Auger effect, in which the energy of an electron transition is absorbed by another electron, which is raised to a higher-energy state in the conduction band, with subsequent emission of the phonons (thermalization); this process is especially important for high concentrations of excess charge carriers; and (3) recombination due to surface states and defects. These process are more difficult to analyze.

2.4 Raman Scattering

Raman effect was discovered by the Indian physicist C. V. Raman in 1928. When a beam of light strikes a medium, most photons are elastically scattered, this is so-called

Rayleigh scattering. In Rayleigh scattering, the emitted photon has the same wavelength as the absorbing photon. In Raman scattering, the energies of the incident and scattered photons are different. Raman spectroscopy is based on the Raman effect, which is the inelastic scattering of photons.⁸ The Raman effect comprises a very small fraction, about 1 in 10^6 , of the incident photons. Comparing with the PL signal, the Raman signal is relatively much weaker as shown in Fig. 2.10.

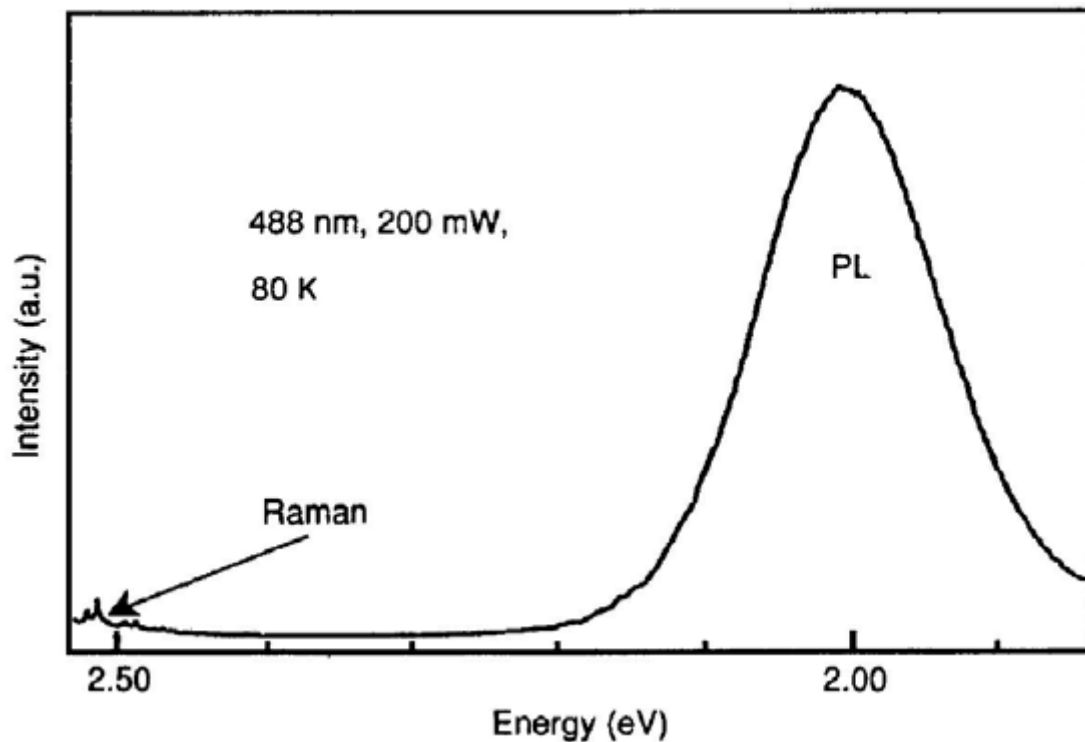


Fig. 2.10

This spectrum showing the photoluminescence peak and the Raman phonon mode of a CdMnTe film on a GaAs substrate (Perkowitz, 1991).

According to quantum theory, we can represent the oscillations of a crystal by phonons, which can be assumed to have discrete energy levels. Therefore, we can

picture light incident on a crystal and interacting with the crystal oscillations as an interaction between a photon and a phonon. When a photon gains energy by absorbing a phonon, we say it anti-Stokes shifted. When the photon loses energy by emission a phonon, we say it is Stokes shifted.⁹ Both of the processes must obey the energy and momentum conservation rules. The conservation conditions can be written as:

$$h\nu_i = h\nu_s \pm h\Omega \quad (2.3)$$

$$\mathbf{k}_i = \mathbf{k}_s \pm \mathbf{K} \quad (2.4)$$

where ν_i and ν_s are the incoming and scattered photon frequencies respectively, \mathbf{k}_i and \mathbf{k}_s are the incoming and scattered photon wave vectors respectively, while Ω and \mathbf{K} are the phonon frequency and wave vector respectively [Fig. 2.11]. The values of frequency shift resulting from Raman scattering range from ten to a few thousand cm^{-1} . Normally speaking, the intensity of the Stokes component is much stronger than that of the anti-Stokes line because usually there are few phonons to be absorbed compared to the number of phonon that can be emitted. Figure 2.12 is a typical Raman spectrum of CCl_4 shows the anti-Stokes shifted and the Stokes shifted. The line at the middle of the figure, denoted by zero, shows the spectral position of the incident monochromatic laser. It also denotes the Rayleigh scattering.

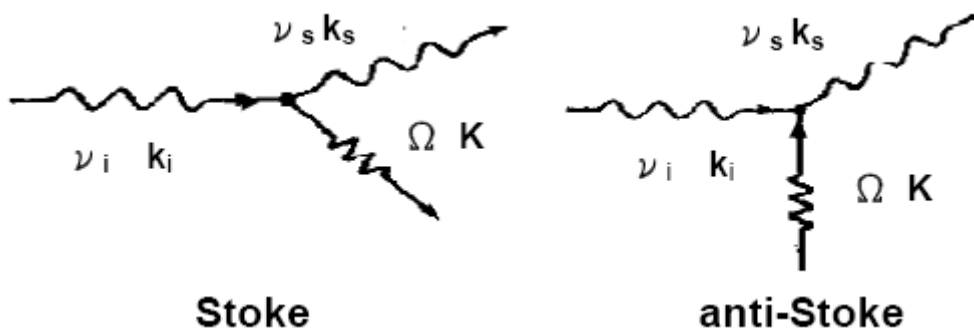


Fig. 2.11

The diagram shows the conservation rules in the Raman scattering.

Raman spectrum of CCl₄

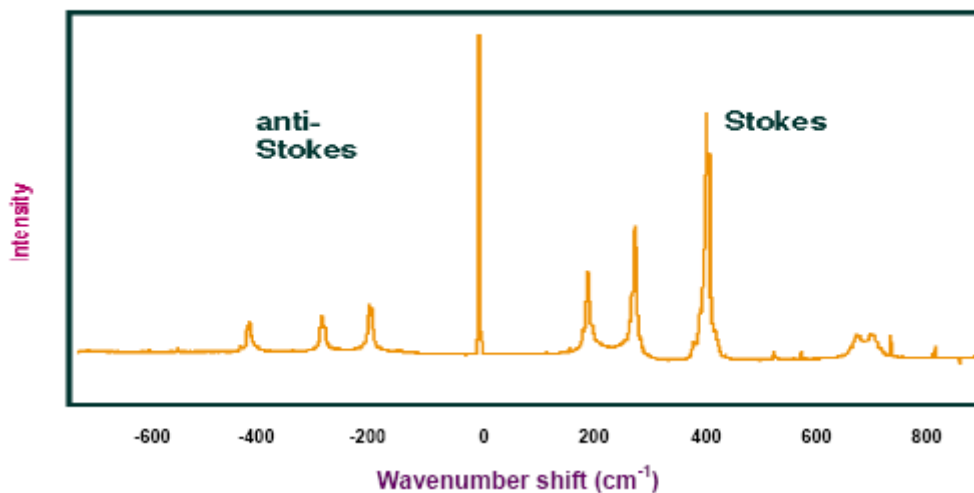


Fig. 2.12

The Raman spectrum of CCl₄.

Through the theoretical calculation, the lattice vibrations can be distinguished to longitudinal acoustic and optical (LA and LO) and transverse acoustic and optical (TA and TO) modes. In a Raman spectrum, the Rayleigh scattering is not shifted, the magnitude of a shift is determined by a optical phonon energy, which is in the range of a

approximately 5 meV to 250 meV, and the energy shift is in the range of 6×10^{-3} meV to 0.1 meV for acoustic phonons. Because the phonon frequencies are so small, the high resolution techniques are needed to detect them. Raman scattering is inherently a weak process, but lasers provide enough power so that the spectra can be routinely measured. Figure 2.13 shows a simplified Raman spectroscopy experiment setup with a charged-coupled device (CCD) as the detector. One thing needs to be emphasized is that those Raman shifts measured are precisely the frequencies of crystal oscillations regardless of the frequency of incident light.

Not every mode can be observed in a Raman spectrum. The Raman scattering must satisfy the selection rules, such as conservation of momentum and energy as well as the point-group selection rules. These originate from the fact that the crystal unit cell is invariant under only a certain set of symmetry operations, and in fact, it is this set of symmetry operations which defines the crystal point group. Similarly, the phonon behavior also has transformation properties. If these transformation properties do not satisfy certain requirements, which depend on the crystal point group, then light will not be scattered. Crystal point-group selection rules are a simple yet powerful way to determine and distinguish between phonon modes of different symmetries.

All the main Raman parameters like band frequencies and intensities, line shape and linewidth, polarization behavior can be used to characterize the lattice, impurities,

and free carriers in a semiconductor. The intensity gives information about crystallinity since it may be reduced in crystals damaged by ion bombardment or other means. The linewidth increases when a material is damaged or disordered because these conditions increase phonon damping or change the rules for momentum conservation in the Raman process. The strengths and frequencies of the Raman phonon bands can determine the degree of alloying in a mixed material. All these capabilities can be used for layered microstructures as well as bulk materials, subject only to the limitation that the penetration depth of the exciting radiation ranges from a few hundreds nanometers to a micrometer. However, a change in the wavelength of the exciting radiation changes the penetration, giving flexibility in the probe depth. The small wavelength of excitation radiation, combined with Raman microprobe technique, also provides good spatial resolution.

Owing to the close relation between Raman scattering and the oscillations of atoms and molecules inside the materials, we can gain the information about the oscillations of atoms and molecules inside the materials from Raman scattering spectrum. These oscillations are mainly controlled by interatomic or intermolecular interactions. Raman-scattering researches can therefore provide a way for people to understand these interaction forces.

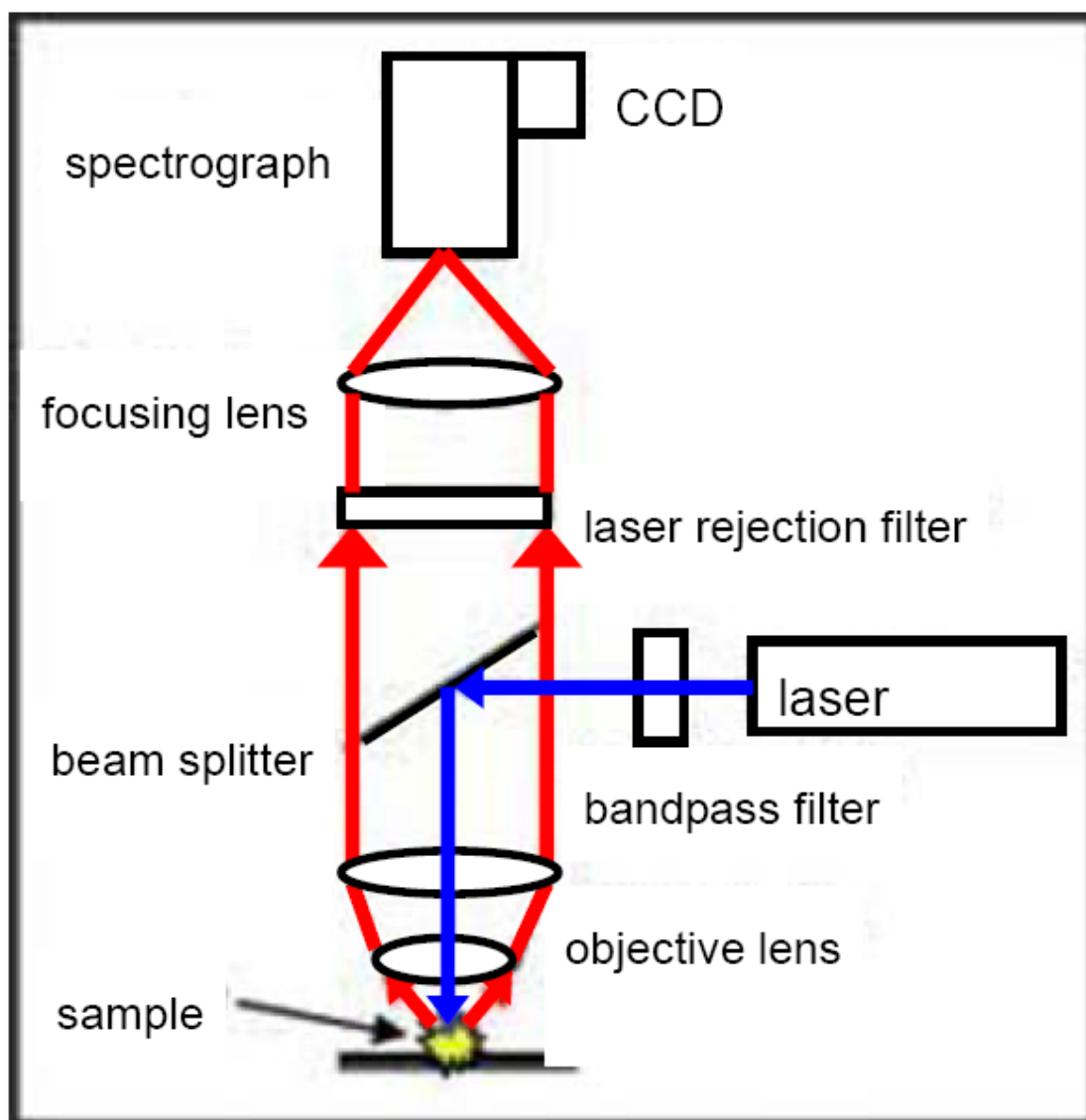


Fig. 2.13

A simplified Raman spectroscopy experiment setup with a charged-coupled device (CCD) as the detector.

2.5 Properties of Deoxyribonucleic Acid (DNA)

DNA is a long polymer made from repeating units called nucleotides.^{10,11} The DNA chain is 22 to 26 Ångströms wide (2.2 to 2.6 nanometers), and one nucleotide unit is 3.3 Å (0.33 nm) long.¹² Although each individual repeating unit is very small, DNA

polymers can be enormous molecules containing millions of nucleotides. For instance, the largest human chromosome, chromosome number 1, is approximately 220 million base pairs long.¹³

In living organisms, DNA does not usually exist as a single molecule, but instead as a tightly-associated pair of molecules.^{14,15} These two long strands entwine like vines, in the shape of a double helix. The nucleotide repeats contain both the segment of the backbone of the molecule, which holds the chain together, and a base, which interacts with the other DNA strand in the helix. In general, a base linked to a sugar is called a nucleoside and a base linked to a sugar and one or more phosphate groups is called a nucleotide. If multiple nucleotides are linked together, as in DNA, this polymer is called a polynucleotide.¹⁶

As shown in Fig. 2.14, the backbone of the DNA strand is made from alternating phosphate and sugar residues.¹⁷ The sugar in DNA is 2-deoxyribose, which is a pentose (five-carbon) sugar. The sugars are joined together by phosphate groups that form phosphodiester bonds between the third and fifth carbon atoms of adjacent sugar rings. These asymmetric bonds mean a strand of DNA has a direction. In a double helix the direction of the nucleotides in one strand is opposite to their direction in the other strand. This arrangement of DNA strands is called antiparallel. The asymmetric ends of DNA strands are referred to as the 5' (five prime) and 3' (three prime) ends, with the 5' end

being that with a terminal phosphate group and the 3' end that with a terminal hydroxyl group. One of the major differences between DNA and RNA is the sugar, with 2-deoxyribose being replaced by the alternative pentose sugar ribose in RNA.¹⁵

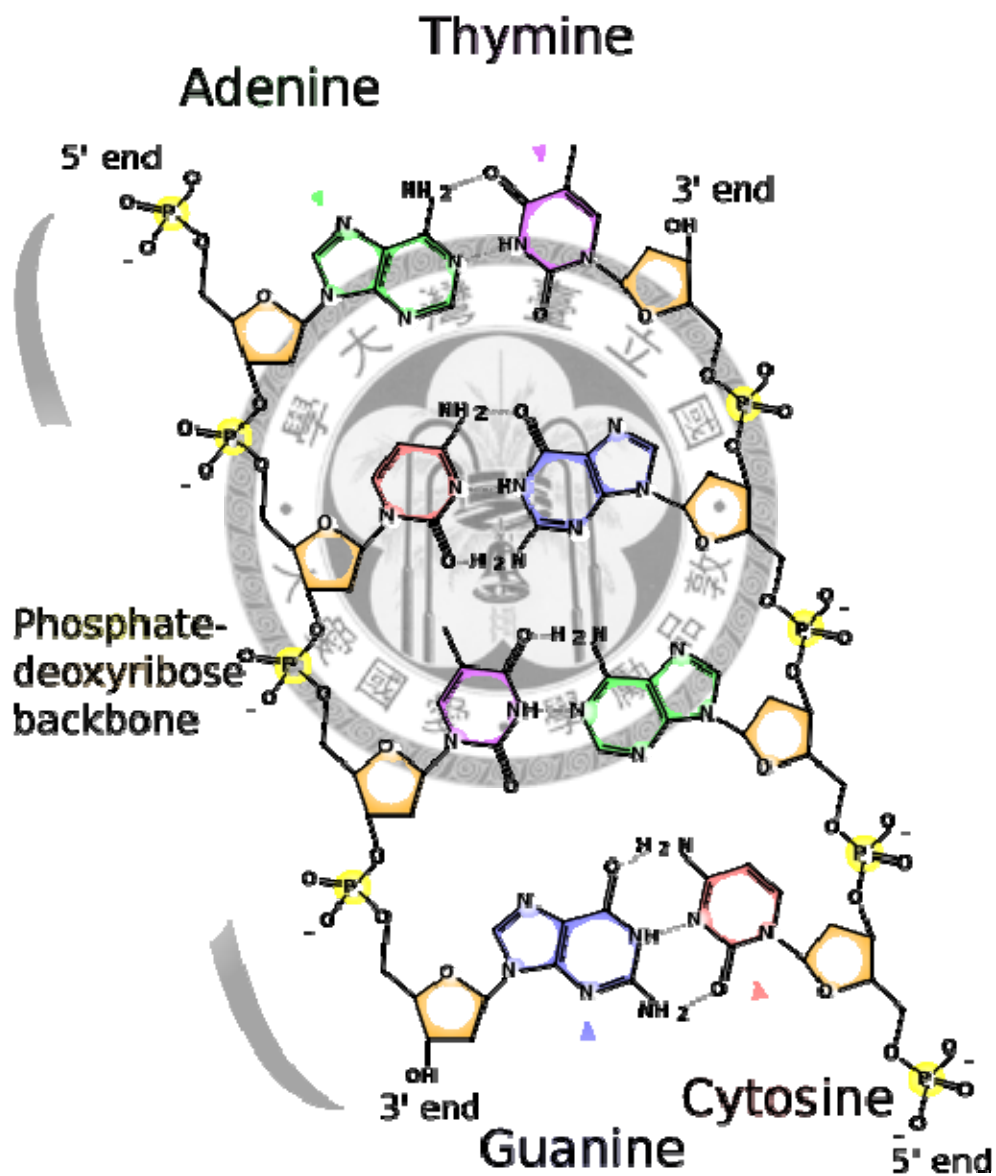


Fig. 2.14

The chemical structure of DNA. Hydrogen bonds are shown as dotted lines.

The DNA double helix is stabilized by hydrogen bonds between the bases attached to the two strands. The four bases found in DNA are adenine (abbreviated A), cytosine (C), guanine (G) and thymine (T). These four bases are attached to the sugar/phosphate to form the complete nucleotide, as shown for adenosine monophosphate.

These bases are classified into two types; adenine and guanine are fused five- and six-membered heterocyclic compounds called purines, while cytosine and thymine are six-membered rings called pyrimidines.¹⁵ A fifth pyrimidine base, called uracil (U), usually takes the place of thymine in RNA and differs from thymine by lacking a methyl group on its ring. Uracil is not usually found in DNA, occurring only as a breakdown product of cytosine.

Here I would like to introduce two basic concepts in addition, (1) major and minor grooves and (2) base pairing:

(1) Major and minor grooves

The double helix is a right-handed spiral. As the DNA strands wind around each other, they leave gaps between each set of phosphate backbones, revealing the sides of the bases inside. There are two of these grooves twisting around the surface of the double helix: one groove, the major groove, is 22 Å wide and the other, the minor groove, is 12 Å wide.¹⁸ The narrowness of the minor groove means that the edges of the bases are more accessible in the major groove. As a result, proteins like transcription

factors that can bind to specific sequences in double-stranded DNA usually make contacts to the sides of the bases exposed in the major groove.¹⁹

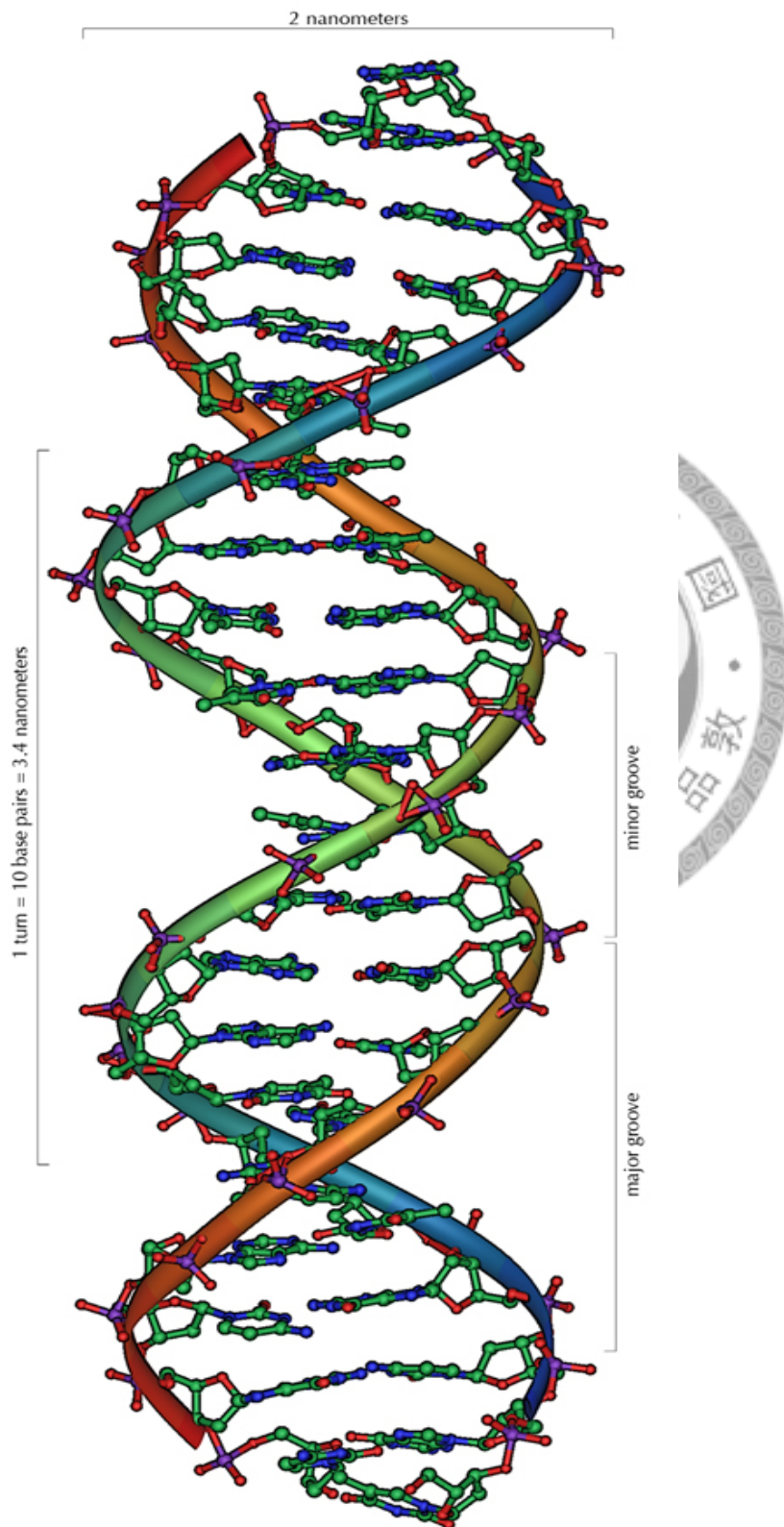


Fig. 2.15
The structure of part of a DNA double helix.

(2) Base pairing

Each type of base on one strand forms a bond with just one type of base on the other strand. This is called complementary base pairing. Here, purines form hydrogen bonds to pyrimidines, with A bonding only to T, and C bonding only to G. This arrangement of two nucleotides binding together across the double helix is called a base pair. The double helix is also stabilized by the hydrophobic effect and pi stacking, which are not influenced by the sequence of the DNA.²⁰ As hydrogen bonds are not covalent, they can be broken and rejoined relatively easily. The two strands of DNA in a double helix can therefore be pulled apart like a zipper, either by a mechanical force or high temperature.²¹ As a result of this complementarity, all the information in the double-stranded sequence of a DNA helix is duplicated on each strand, which is vital in DNA replication. Indeed, this reversible and specific interaction between complementary base pairs is critical for all the functions of DNA in living organisms.¹⁰

The two types of base pairs form different numbers of hydrogen bonds, AT forming two hydrogen bonds, and GC forming three hydrogen bonds (see figures, left). The GC base pair is therefore stronger than the AT base pair. As a result, it is both the percentage of GC base pairs and the overall length of a DNA double helix that determine the strength of the association between the two strands of DNA. Long DNA helices with a high GC content have stronger-interacting strands, while short helices with high AT

content have weaker-interacting strands.²² In biology, parts of the DNA double helix that need to separate easily, such as the TATAAT Pribnow box in some promoters, tend to have a high AT content, making the strands easier to pull apart.²³ In the laboratory, the strength of this interaction can be measured by finding the temperature required to break the hydrogen bonds, their melting temperature (also called T_m value). When all the base pairs in a DNA double helix melt, the strands separate and exist in solution as two entirely independent molecules. These single-stranded DNA molecules have no single common shape, but some conformations are more stable than others.²⁴

2.6 Scanning Electron Microscopy

Electron microscope utilizes an electron beam (e-beam) to produce a magnified image of the sample. There are three principle types of electron microscopes: scanning, transmission, and emission. In the scanning and transmission microscope, an e-beam incident on the sample produces an image while in the field-emission microscope the specimen itself is the source of electrons. Scanning electron microscopy (SEM) is similar to light microscopy with the exception that electrons are used instead of photons and the image photons and the image is formed in a different manner. A SEM consists of an electron gun, a lens system, scanning coils, an electron collector, and a cathode ray display tube (CRT). The electron energy is typically 10-30 KeV for most samples,

but for insulating samples the energy can be as low as several hundred eV. The use of electrons has two main advantages over typical microscopes: much larger magnifications are possible since electron wavelengths are much shorter than the photon wavelengths and the depth of field is much higher.

De Broglie proposed in 1923 that particles can also behave as waves. The electron wavelength λ_e depends on the electron velocity v or the accelerating voltage V as

$$\lambda_e = \frac{h}{mv} = \frac{h}{\sqrt{2qmV}} = \frac{1.22}{\sqrt{V}} \text{ (nm)} \quad (2.5)$$

The wavelength is 0.012 nm for $V=10000$ (v) - a wavelength significantly below the 400 to 700 nm wavelength range of visible light – making the resolution of an SEM much better than that of an optical microscope.

The contrast in a SEM depends on a number of factors. For a flat, uniform sample the image shows on contrast. If, however, the sample consists of materials with different atomic numbers, a contrast is observed if the signal is obtained from the backscattered electrons, because the backscattering coefficient increases with the atomic number Z .

The secondary electron emission coefficient, however, is not a strong function of Z and atomic number variations give no appreciable contrast. Contrast is also influenced by the surface conditions and by the local electric field. But the main contrast-enhancing feature is the sample topography. Secondary electrons are emitted from the top 10 nm or so of the sample surface. When the sample surface is tilted from the normal beam

incidence, the electron beam path lying within this 10 nm is increased by the factor $1/\cos\theta$, where θ is the angle from the normal incidence ($\theta = 0^\circ$ for normal incidence). The interaction of the incident beam with the sample increases with path length and the secondary electron emission coefficient increases. The contrast C depends on the angle as

$$C = \tan(\theta)d\theta \quad (2.6)$$

For $\theta = 45^\circ$, a change in the angle of $d\theta = 1^\circ$ produces a contrast of 1.75% while at 60° the contrast increase to 3% for $d\theta = 1^\circ$.

The beam diameter of SEMs is in the range of 1 to 10 nm. Yet the resolution of e-beam measurements is not always that good. Why is that? It has to do with the shape of the electron-hole cloud generated in the semiconductor. When electrons impinge on a solid, they lose energy by elastic scattering (change of direction with negligible energy loss) and inelastic scattering (energy loss with negligible change in direction). Elastic scattering is caused mainly by interactions of electrons with nuclei and is more probable in high atomic number materials and at low beam energies. Inelastic scattering is caused mainly by scattering from valence and core electrons. The result of these scattering events is a broadening of the original nearly collimated, well-focused electron beam within the sample.

The generation volume is a function of the e-beam energy and the atomic number

Z of the sample. Secondary electrons, backscattered electrons, characteristic and continuum X-rays, Auger electrons, photons, and electron-hole pairs are produced. For low-Z samples most electrons penetrate deeply into the sample and are absorbed. For high-Z samples there is considerable scattering near the surface and a large fraction of the incident electrons is backscattered. The shape of the electron distribution is “teardrop”-shaped, as shown in Fig. 2.16. As Z increase ($15 < Z < 40$) the shape becomes more spherical and for $Z > 40$ it becomes hemispherical. “Teardrop” shapes have been observed by exposing polymethylmethacrylate to an electron beam and etching the exposed portion of the material. Electron trajectories, calculated with Monte Carlo techniques, also agree with these shapes.

The depth of electron penetration is the electron range R_e , defined as the average total distance from the sample surface that an electron travels in the sample along a trajectory. A number of empirical expressions have been derived for R_e . One such expression is

$$R_e = \frac{4.28 \times 10^{-6} E^{1.75}}{\rho} \text{ (cm)} \quad (2.7)$$

where ρ is the sample density (g/cm^3) and E the electron energy (KeV).

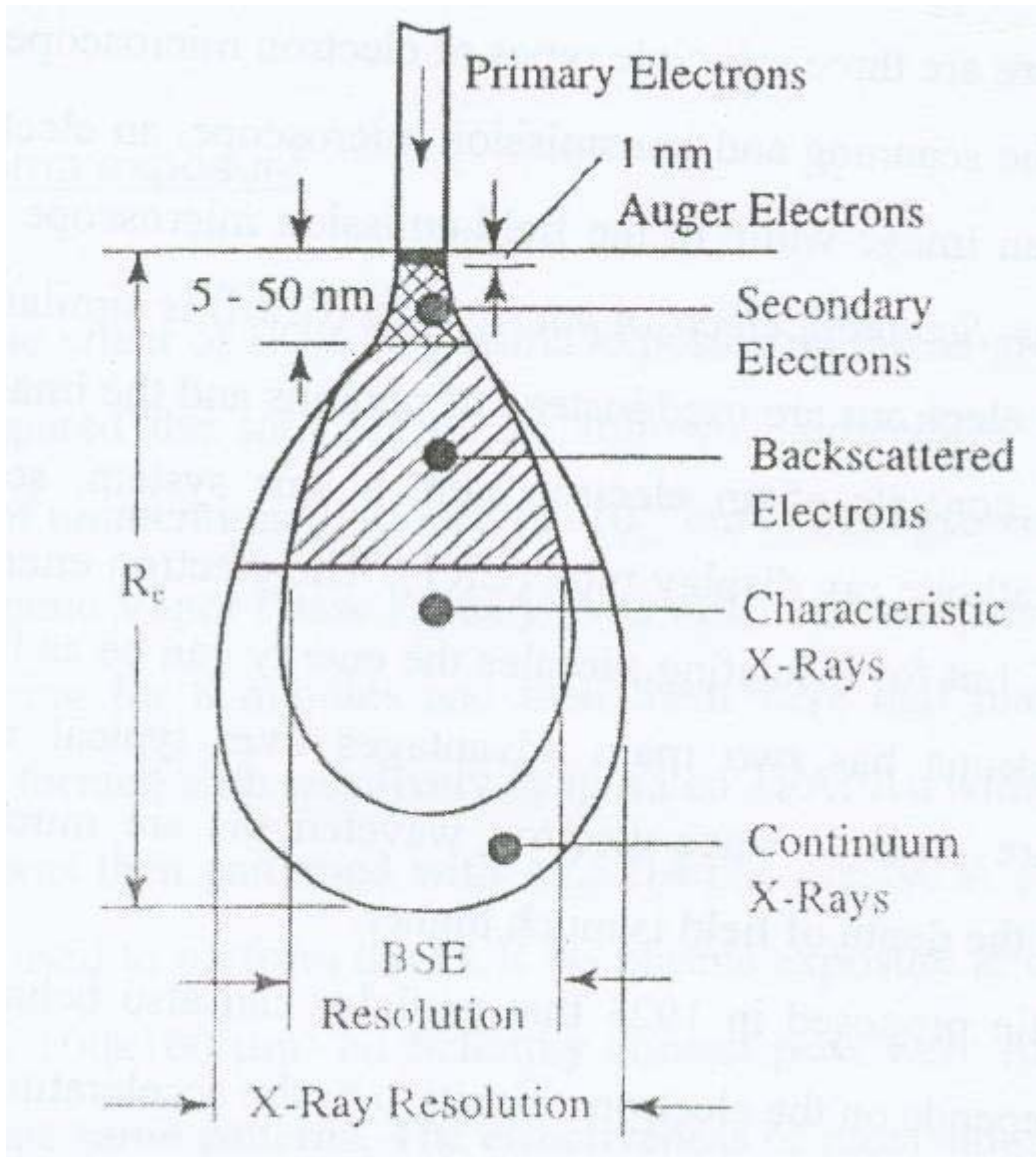


Fig. 2.16

Summary of the range and spatial resolution of backscattered electrons, secondary electrons, X-rays, and Auger electrons for electrons incident on a solid.

References

1. Gerald B. Stringfellow, *Organometallic Vapor-Phase Epitaxy: Theory and Practice (2nd ed.)*, Academic Press (1999) (ISBN 0-12-673842-4).
2. R.S. Wagner and W.C. Ellis, *Applied Physics Letters* **4**, 89 (1964).
3. M. Quirk and J. Serda, *Semiconductor Manufacturing Technology*, Prentice Hall (2000).
4. R. A. Stradling and P. C. Klipstein, *Growth and Characterisation of Semiconductors*, published by Hilger (1990).
5. S. Perkowitz, *Optical Characterization of Semiconductors: Infrared, Raman, and Photoluminescence Spectroscopy*, published by Academic Press (1993).
6. J. I. Pankove, *Optical Processes in Semiconductors*, Prentice-Hall, Inc. (1971).
7. G. D. Gilliland, *Mater. Sci. Eng.* **R18**, 99 (1997)
8. P. Y. Yu and M. Cardona, *Fundamentals of Semiconductors*, published by Springer (2001).
9. C. V. Raman, *Nature* **121**, 619 (1928).
10. Alberts Bruce, Alexander Johnson, Julian Lewis, Martin Raff, Keith Roberts, and Peter Walters, *Molecular Biology of the Cell, Fourth Edition*. New York and London, Garland Science. (2002).ISBN 0-8153-3218-1.
11. Butler and John M, *Forensic DNA Typing*, Elsevier. (2001).ISBN

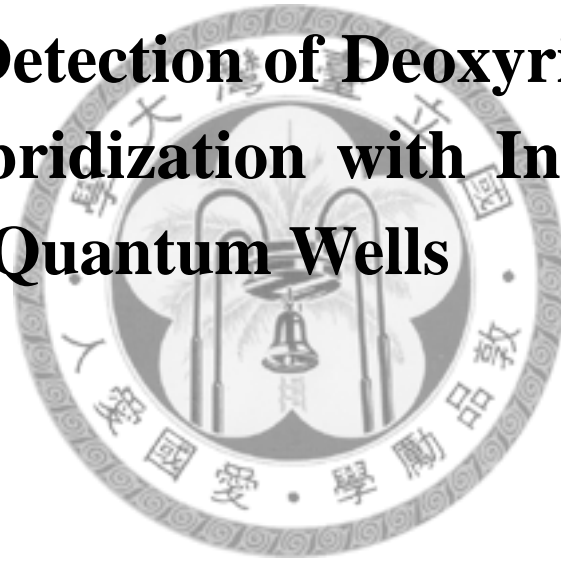
978-0-12-147951-0.

12. Mandelkern M, Elias J, Eden D, and Crothers D. "The dimensions of DNA in solution". *J Mol Biol* **152** (1): 153–61(1981).
13. Gregory S, et al.. "The DNA sequence and biological annotation of human chromosome 1". *Nature* **441** (7091), 315–21(2006).
14. Watson J, Crick F. "Molecular structure of nucleic acids; a structure for deoxyribose nucleic acid". *Nature* **171** (4356): 737–8(1953).
15. Berg J., Tymoczko J. and Stryer L., *Biochemistry*, W. H. Freeman and Company (2002), ISBN 0-7167-4955-6.
16. G. P. Moss, *Abbreviations and Symbols for Nucleic Acids, Polynucleotides and their Constituents*, IUPAC-IUB Commission on Biochemical Nomenclature (CBN), Accessed 03 Jan 2006
17. Ghosh A, Bansal M. "A glossary of DNA structures from A to Z", *Acta Crystallogr D Biol Crystallogr* **59** (Pt 4), 620-6(2003).
18. Wing R, Drew H, Takano T, Broka C, Tanaka S, Itakura K, Dickerson R. "Crystal structure analysis of a complete turn of B-DNA". *Nature* **287** (5784): 755–8 (1980).
19. Pabo C, Sauer R. "Protein-DNA recognition". *Annu Rev Biochem* **53**: 293–321 (1984).

20. Ponnuswamy P, Gromiha M. "On the conformational stability of oligonucleotide duplexes and tRNA molecules". *J Theor Biol* **169** (4): 419–32 (1994).
21. Clausen-Schaumann H, Rief M, Tolksdorf C, Gaub H. "Mechanical stability of single DNA molecules". *Biophys J* **78** (4): 1997–2007 (2000).
22. Chalikian T, Völker J, Plum G, Breslauer K. "A more unified picture for the thermodynamics of nucleic acid duplex melting: a characterization by calorimetric and volumetric techniques". *Proc Natl Acad Sci USA* **96** (14): 7853–8 (1999).
23. deHaseth P, Helmann J. "Open complex formation by Escherichia coli RNA polymerase: the mechanism of polymerase-induced strand separation of double helical DNA". *Mol Microbiol* **16** (5): 817–24 (1995).
24. Isaksson J, Acharya S, Barman J, Cheruku P, Chattopadhyaya J. "Single-stranded adenine-rich DNA and RNA retain structural characteristics of their respective double-stranded conformations and show directional differences in stacking pattern". *Biochemistry* **43** (51): 15996–6010 (2004).
25. C. Kittel, *Introduction to Solid State Physics (Seventh Edition)*.
26. B. V. Zeghbroeck, *Principles of Semiconductor Devices* (boulder, 1997).
27. J. R. Lakowicz, *Principles of Fluorescence Spectroscopy* (Academic, New York 1999).

Chapter 3

Optical Detection of Deoxyribonucleic Acid Hybridization with InGaN/GaN multiple Quantum Wells



Chapter 3

Optical Detection of Deoxyribonucleic Acid Hybridization with InGaN/GaN multiple Quantum Wells

3.1 Introduction

Nowadays, research and development of biosensors have become important topics in genetic engineering, such as genetic identification of certain infectious or inherited diseases as well as cancers.¹ Various methods of deoxyribonucleic acid (DNA) or ribonucleic acid (RNA) base-sequence identification have been published widely.² The hybridization detection of single-stranded probe DNA and target DNA is one of the main concepts of base-sequence identification techniques.³⁻⁶ Usually, single-stranded DNA (ssDNA) molecules as probes are immobilized onto the surface of some materials, and then the target ssDNA, matched and mismatched, respectively, are injected into the buffer solution where the probe-DNA-surface located. As the hybridization of matched target ssDNA and probe ssDNA occurs, the mass or charge distribution on the material surface will be altered, thus the corresponding properties of the underlying material will be changed. If the mismatched target DNA solution is injected, the properties will remain the same because the hybridization process does not occur. Accordingly, biologically modified field effect transistors (FETs) have been developed to directly

detect biochemical interactions for a variety of applications.⁷⁻¹⁰ However, in the FET related techniques, ones often consume much time in constructing electronic structures such as ohmic contacts, junctions and electrodes, and in some cases it is not convenient to do the electric current measurements.⁷⁻¹¹

$\text{In}_x\text{Ga}_{1-x}\text{N}/\text{GaN}$ multiple quantum wells (MQWs) have been widely used for the application of light emitting devices (LED) and laser diodes. If the biosensor is made based upon the change of the optical properties of nitride MQWs optical devices, it will have a great advantage for practical applications. It is known that nitride semiconductors are good piezoelectric (PZ) material. Due to the inherent nature of wurtzite crystalline structure and lattice mismatch, $\text{In}_x\text{Ga}_{1-x}\text{N}/\text{GaN}$ MQWs consist of large spontaneous and piezoelectric polarizations, which can significantly alter their physical properties. Because both of spontaneous and piezoelectric polarizations are very sensitive to the surface environment, functionalized nitride MQWs devices therefore offer a very good opportunity to serve as a highly sensitive sensor. Indeed, electrical detection of immobilized proteins with ungated AlGaN/GaN transistors has been demonstrated recently.⁷ Instead of using electric current detection, here we demonstrate a novel alternative that the optical properties of functionalized InGaN/GaN MQWs also provide an excellent opportunity to serve as sensitive biosensors.

3.2 Experiment

The studied InGaN/GaN MQWs were prepared by low-temperature metal-organic chemical vapor deposition. An undoped series of ten periods of 2-nm-thick $\text{In}_{0.22}\text{Ga}_{0.78}\text{N}$ well and 9-nm-thick GaN barriers were grown on (0001) sapphire. There is a 6 μm n-GaN layer between sapphire and MQWs. Micro-photoluminescence ($\mu\text{-PL}$) measurements were performed at room temperature in backscattering geometry by Jobin Yvon T64000 system working in the triple-subtractive mode. The incident and scattered light propagated parallel to the c -axis, which in turn was normal to the growth surface. The sample was excited by a continuous wave (cw) He–Cd laser working at 325 nm, and a neutral density filter was used to control the laser intensity. Raman scattering measurements were also performed by the same experimental system, while the pumping source was switched to 488 nm (2.55 eV) radiation from a Ar^+ laser.

As shown in Fig. 3.1, for the construction of the probe chip, we first sputtered a 5 nm-Au layer onto a clean InGaN/GaN MQWs surface, which was then exposed to a solution of 1 μM single-stranded probe DNA with thiol modification (thiol- $(\text{CH}_2)_3$ -5'-TGTAGTAGTGTTGTT-3') in the phosphate buffered saline (PBS) solution for 12 hours in room temperature. A monolayer of ssDNA was absorbed onto the Au surface by reaction with thiol modification due to strong interaction between Au and the thiol group.¹⁰ Next, the sample was exposed to a 1 μM 6-Mercapto-1-hexanol

(MCH) solution for composition of a spacer for 3 hours. Finally, the sample was washed with buffer solution.

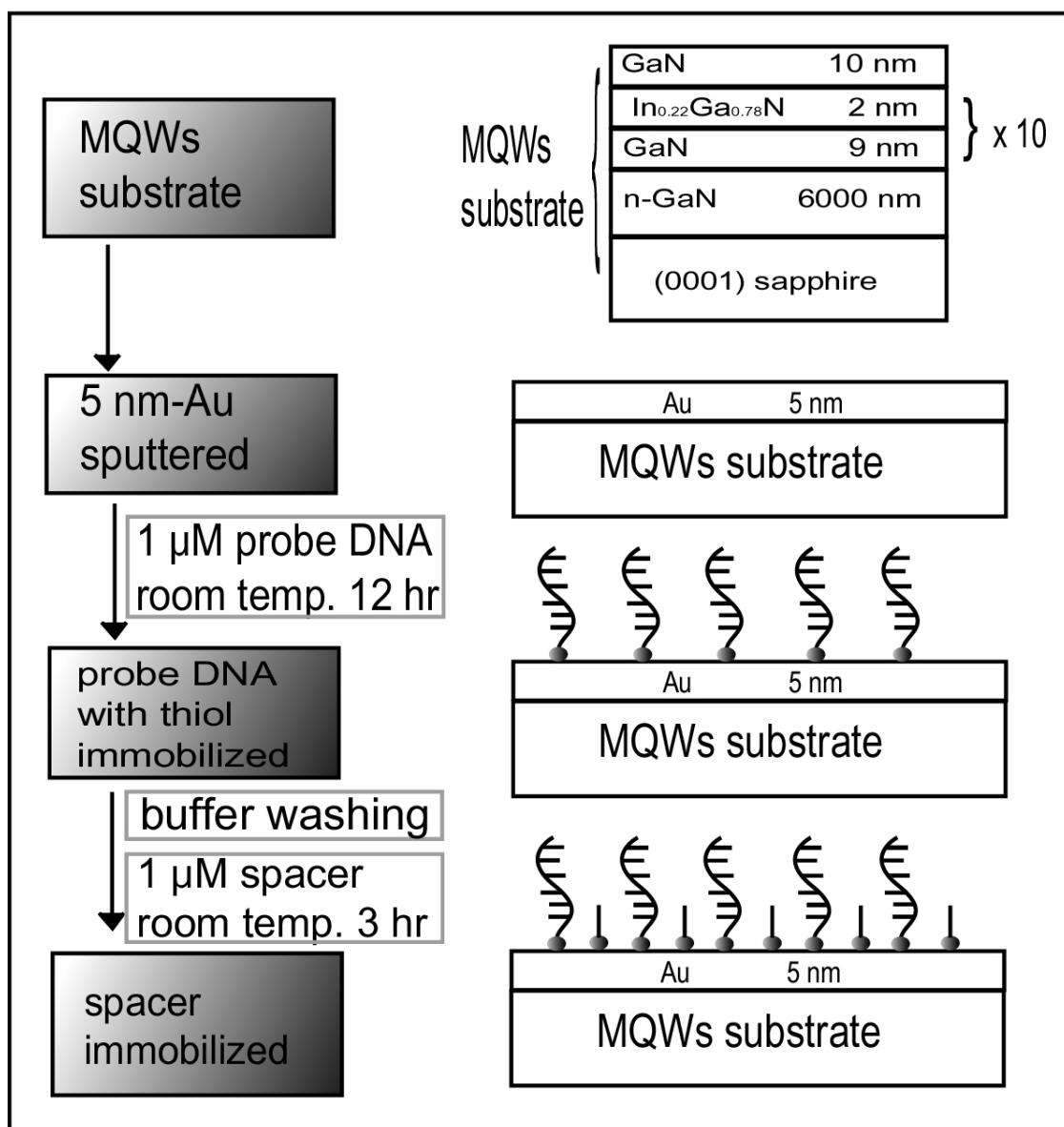


Fig. 3.1

Procedure for the construction of a probe chip. We first sputtered a 5-nm-Au layer onto the MQWs substrate, and then probe DNA molecules with thiol were immobilized onto the Au surface. Finally, MCH solution was injected as spacer molecules.

3.3 Results and Discussion

In order to demonstrate the influence on the optical properties of InGaN/GaN MQWs due to the change of spontaneous and piezoelectric polarizations, in the beginning we have performed μ -PL spectra under different optical excitation densities as shown in Fig. 3.2(a). Each spectrum in Fig. 3.2(a) is dominated by the emission at around 2.8 eV arising from the excitonic transition of InGaN quantum wells.^{12,13} We can clearly see that the peak position shifts toward the high energy side as the excitation power increases. This behavior can be well understood according to the quantum confined Stark effect (QCSE).^{12,13} Because there exist both spontaneous and piezoelectric polarizations in InGaN MQWs, which will induce a strong internal electric field in the quantum well and tilt the band alignment as shown in Fig. 3.2(b). With the increase of pumping power density, the screening of the internal electric field due to photoexcited electron-hole pairs is more effective, and the tilting of the band structure becomes less pronounced. It thus leads to the increase in the transition energy and the blueshift of the observed spectra.

To detect the hybridization process, we immersed the probe chip into the buffer solution and then matched and mismatched target ssDNA were injected. Figure 3.3 shows the μ -PL spectra of the probe chip in target DNA solution with different

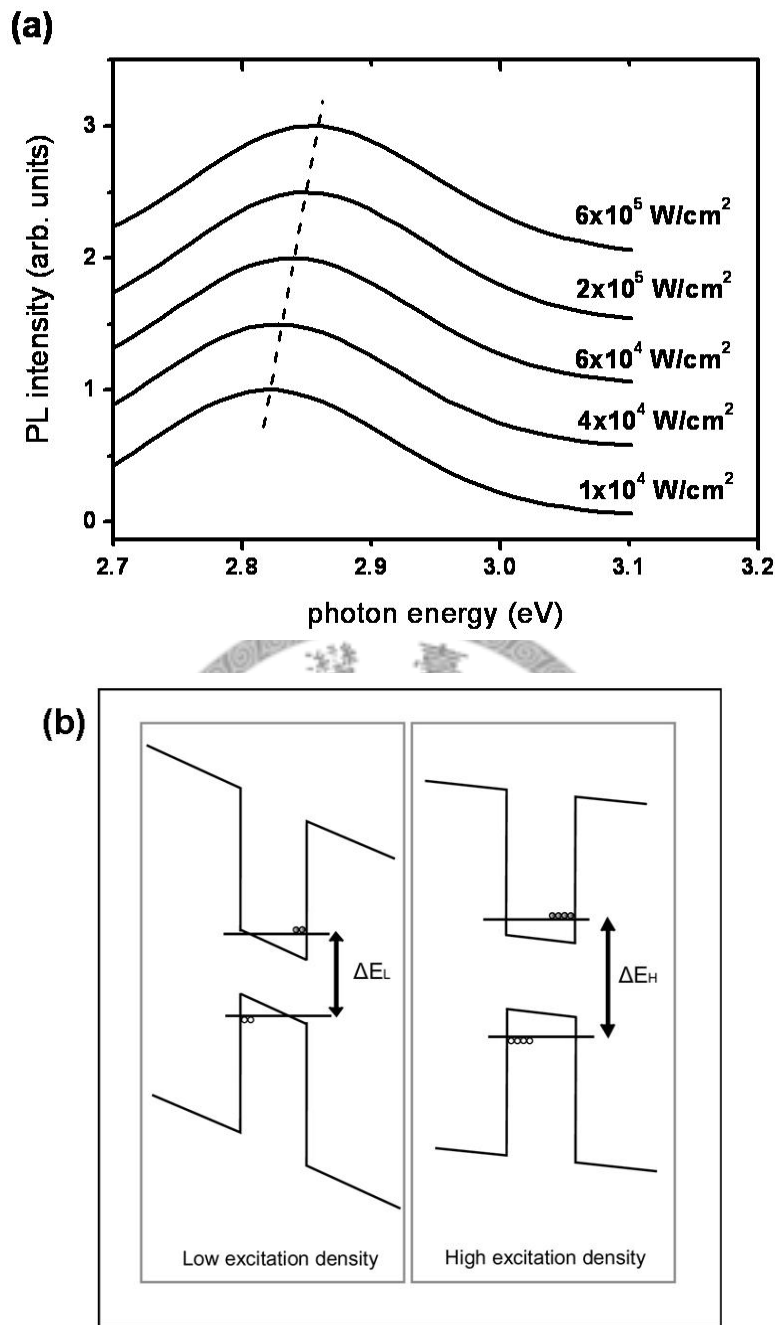


Fig. 3.2

(a) PL spectra from InGaN/GaN MQWs sample under different optical excitation densities. The peak shows a blue shift as the excitation power increases due to the spontaneous and piezoelectric polarizations and quantum confined Stark effect. (b) Band structure of InGaN/GaN quantum wells. It shows that the recombination energy of electron-hole pairs is higher in a flatter quantum well.

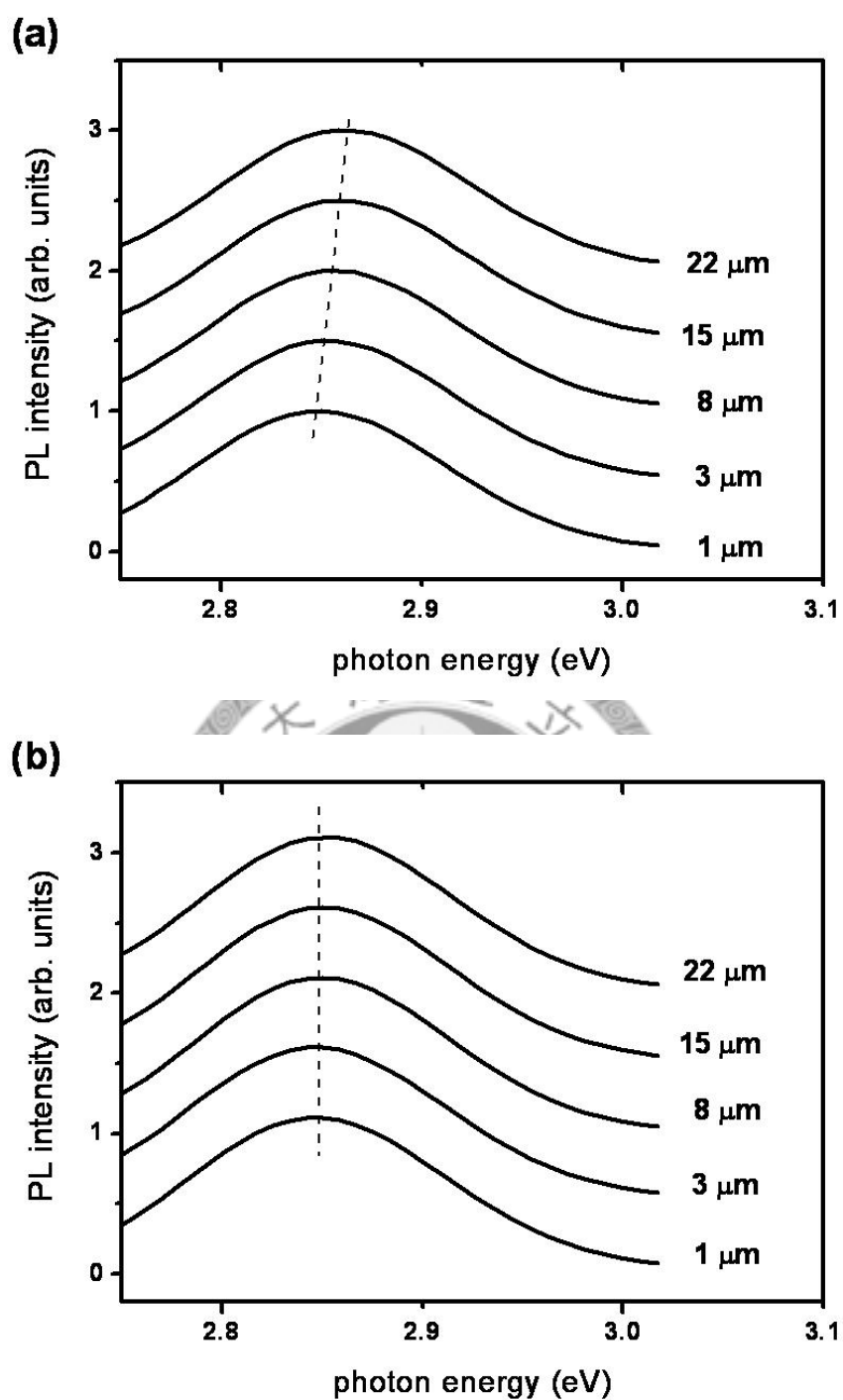


Fig. 3.3

PL spectra from the probe chip in target DNA solution with different concentrations. (a) The peak position shifts toward the high energy side as the matched target DNA concentration increases, while (b) the PL spectra of the mismatched target DNA remain the same.

concentrations. Each measurement was taken after the target DNA injection for 10 minutes to ensure that most target DNA can react with the probe chip. It is clear that the peak position of PL spectra shifts toward the high energy side as the matched target DNA (5'-AACAACTACTACA-3') concentration increases, while the PL spectra of the mismatched target DNA remain the same. We attribute the spectral shift to the hybridization of the target ssDNA and the probe ssDNA that immobilized on the Au surface. Because the surface charge distribution of the probe chip is altered due to the hybridization process, which changes the surface polarization, in turn the built-in internal electric field is changed. The modification of the internal electric field then reflects in the tilting of the band alignment and therefore the PL spectra.

To further confirm the above interpretation, we have performed Raman scattering measurements for different concentrations of target ssDNA solution as shown in Fig.3.4. The broaden line located near 735 cm^{-1} can be assigned to InGaN $A_1(\text{LO})$ mode^{14,15}, which shows a clear low-energy shift in the peak position with respect to the increase of the matched target DNA concentration, while the spectra corresponding to the mismatched target DNA remain unchanged. The low-energy shift of the Raman scattering spectra can not be attributed to the laser heating, because the experimental condition was kept the same for both of the matched and mismatched target DNAs.

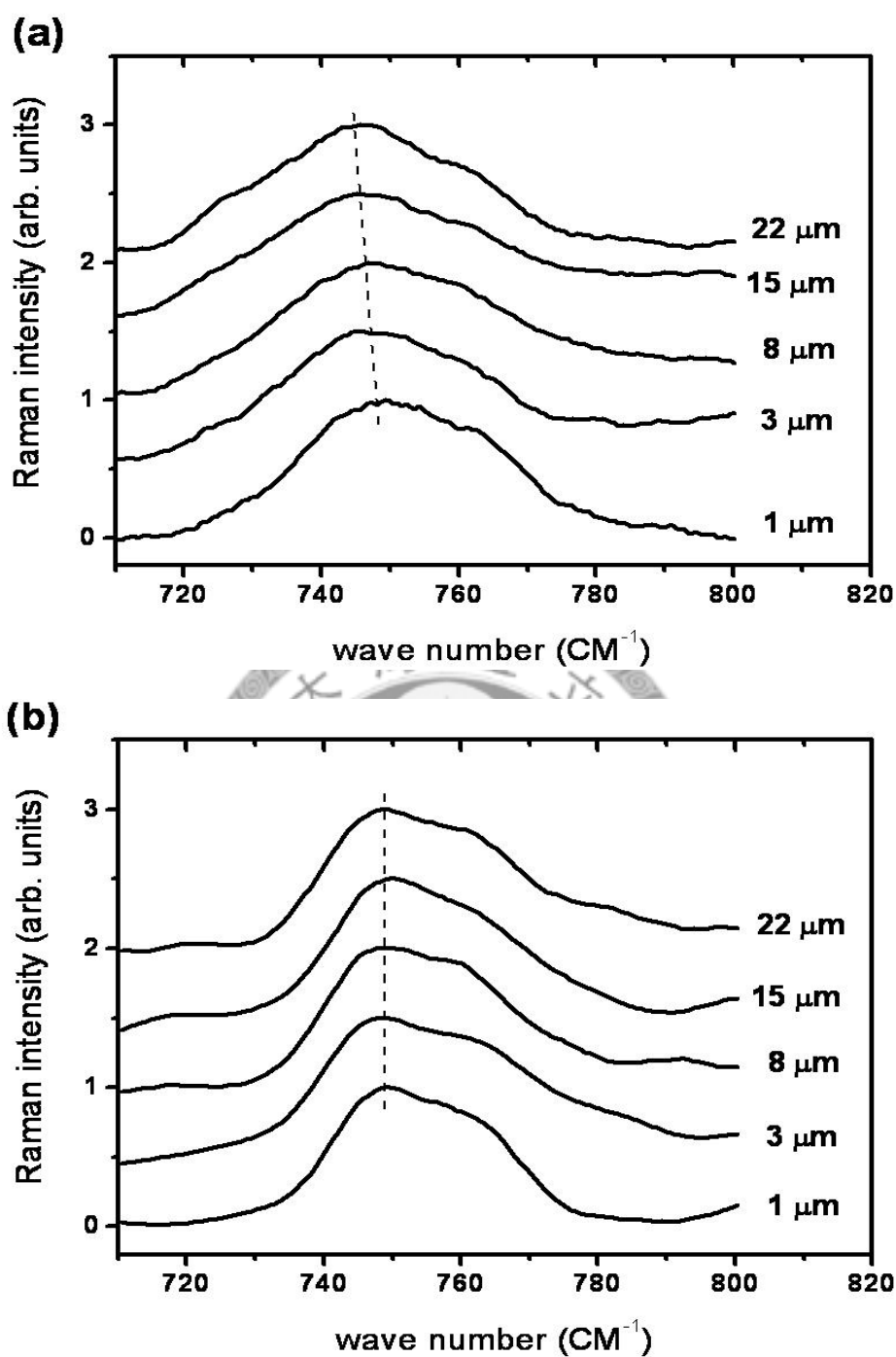


Fig. 3.4

The $A_1(\text{LO})$ phonon in Raman scattering spectra from the probe chip in target DNA solution with different concentrations. (a) The phonon energy shows a low-energy shift with the increase of matched target DNA concentration, while (b) the spectra corresponding to the mismatched target DNA do not change.

This intriguing behavior can also be understood in terms of the modification of internal electric field arising from the hybridization of target and probe DNAs as described above. Because nitride semiconductors are good piezoelectric material, a change in the internal electric field can produce a strain and alter the lattice constant, which then leads to the change of the Raman scattering spectra.¹⁶ According to the PL spectra shown in Fig. 3.3(a), the internal electric field is reduced after DNA hybridization, and therefore a low-frequency shift of the LO phonon energy should be expected. This prediction is just consistent with what has been observed as shown in Fig. 3.4(a).

To further confirm our results, we have examined the internal strain based upon the Raman scattering measurements. The magnitude of the strain can be estimated by the low-energy shift of the $A_1(\text{LO})$ phonon mode according to the following equation:¹⁷

$$\varepsilon = \frac{\Delta\omega}{2\left(a - b \frac{C_{13}}{C_{33}}\right)}, \quad (3.1)$$

where a and b are phonon deformation potentials, and C_{13} and C_{33} are elastic constants, respectively. Figure 3.5 shows the strain as a function of excitation density calculated from Eq. (3.1), where the deformation potentials a , b and the elastic constants C_{13} , C_{33} were estimated by the extrapolation of the data for GaN and InN.¹⁸ The value of the calculated strain has the same order of magnitude as that reported previously.¹⁸

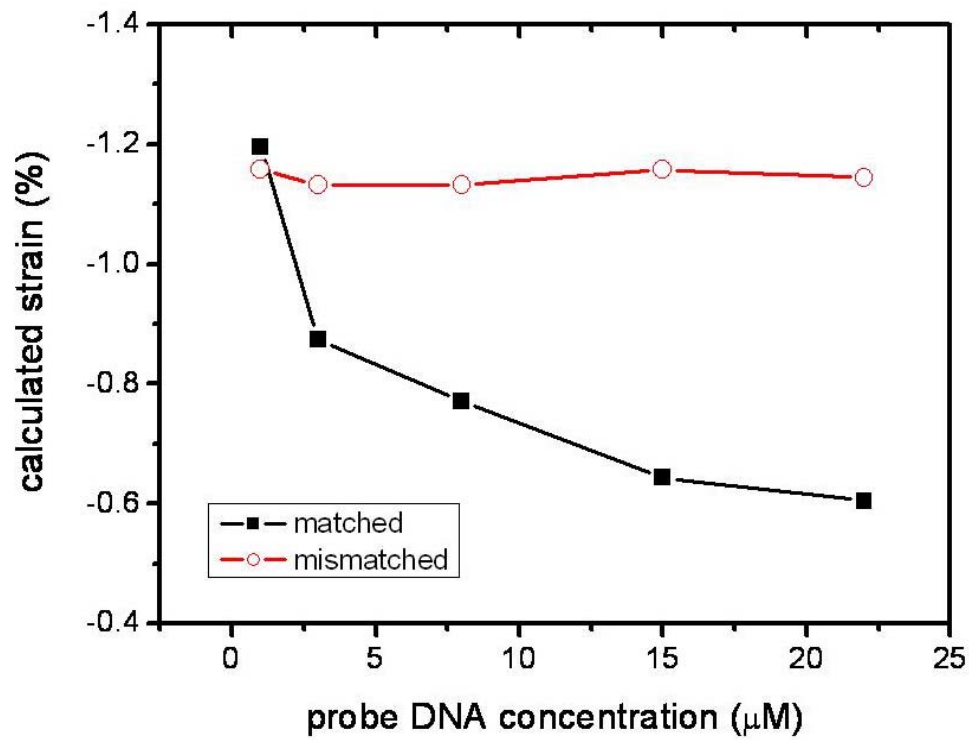


Fig. 3.5

Calculated strain of InGaN/GaN MQWs in the probe chip as a function of target DNA concentration based on Eq. (1). The hybridization process alters the strain of InGaN/GaN MQWs in matched DNA solution, while the MQWs' strain remain unchanged in mismatched DNA solution.

Evidently, the strain of InGaN/GaN MQWs in matched DNA solution decreases with increasing DNA concentration as expected. We therefore can see that the shifts in both PL spectra and Raman scattering of the probe chip can be well explained in a consistent way based on the strain alteration due to the DNA hybridization.

3.4 Conclusion

In conclusion, we have demonstrated that the optical properties of nitride MQWs can be used to detect the hybridization of DNA molecules. The underlying mechanism is based on the highly sensitive nature of both spontaneous and piezoelectric polarizations on surface environment, and nitride semiconductors are good piezoelectric materials. Our working principle shown here can be readily extended by employing many other biomolecules for surface functionalization and by using different chemistries. In view of the wide application of LEDs and laser diodes based on nitride semiconductors, the study carried out along our guideline should be very useful and timely.

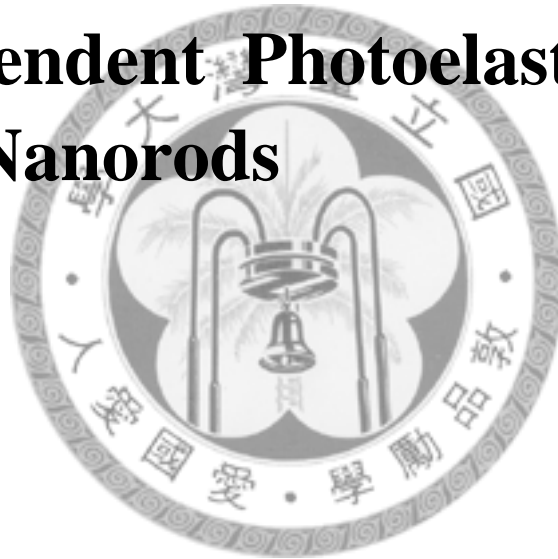
References

1. K. Skogerboe, *Anal. Chem.* **65**, 416R (1993).
2. T. Rajh, Z. Saponjic, J. Liu, N. M. Dimitrijevic, N. F. Scherer, M. Vega-Arroyo, P. Zapol, L. A. Curtiss, and M. C. Thurnauer, *Nano Lett.* **4**, 1017 (2004).
3. I. J. Ticono, *J. Phys. Chem.* **100**, 13311 (1996).
4. R. Drmanac, S. Drmanac, B. Koop, L. Hood, and R. Crkvenjakov, *Science* **260**, 1649 (1993).
5. K. A. Peterlinz, R. M. Georgiadis, T. M. Herne, and M. J. Tarlov, *J. Am. Chem. Soc.* **119**, 3401 (1997).
6. J. J. Storhoff and C. A. Mirkin, *Chem. Rev. (Washington, D.C.)* **99**, 1849 (1999).
7. B. S. Kang, F. Ren, L. Wang, C. Lofton, Weihong W. Tan, S. J. Pearton, A. Dabiran, A. Osinsky, and P. P. Chow, *Appl. Phys. Lett.* **87**, 023508 (2005).
8. G. Xuan, J. Kolodzey, V. Lapoor, and G. Gonye, *Appl. Phys. Lett.* **87**, 103903 (2005).
9. D.-S. Kim, H.-J. Park, H.-M. Jung, J.-K. Shin, P. Choi, J.-H. Lee, and G. Lim, *Jpn. J. Appl. Phys., Part 1* **43**, 3855 (2004).
10. B. S. Kang, S. J. Pearton, J. J. Chen, F. Ren, J. W. Johnson, R. J. Therrien, P. Rajagopal, J. C. Roberts, E. L. Piner, and K. J. Linthicum, *Appl. Phys. Lett.* **89**, 122102 (2006).

11. Hiromasa Tokudome, Yoko Yamada, Shuji Sonezaki, Hiroshi Ishikawa, Makoto Bekki, Koki Kanehira, and Masahiro Miyauchi, Appl. Phys. Lett. **87**, 213901 (2005).
12. T. Y. Lin, Appl. Phys. Lett. **82**, 880 (2003).
13. C. H. Chen, W. H. Chen, Y. F. Chen, and T.Y. Lin, Appl. Phys. Lett. **83**, 1770 (2003).
14. H. Siegle, G. Kaczmarczyk, L. Fillippidis, A. P. Litvinchuk, A. Hoffmann, and C. Thomsen, Phys. Rev. B **55**, 7000 (1997).
15. J. Wagner, A. Ramakrishnan, H. Obloh, and M. Maier, Appl. Phys. Lett. **74**, 3863 (1999)
16. C. F. Klingshirn, *Semiconductor Optics* (Springer, Berlin, 1995).
17. F. C. Wang, C. L. Cheng, Y. F. Chen, C. F. Huang, and C. C. Yang, Semicond. Sci. Technol. **22**, 896 (2007).
18. A.G. Kontos, Y. S. Raptis, N. T. Pelekanos, A. Georgakilas, E. Bellet-Amalric, and D. Jalabert, Phys. Rev. B, **72**, 155336 (2005)

Chapter 4

Size-dependent Photoelastic Effect in ZnO Nanorods



Chapter 4

Size-dependent Photoelastic Effect in ZnO Nanorods

4.1 Introduction

ZnO has been extensively studied due to its unique optical properties in the ultraviolet (UV) region as well as a large exciton binding energy of 60 meV, which holds the promise for producing efficient room-temperature exciton emitters and very low-threshold lasers. The great attention arises not only from the availability in fairly high-quality bulk, but also from much simpler crystal-growth technology exists, resulting in potentially lower costs for ZnO based devices.^{1,2} Recently, quasi-one-dimensional nanoscale ZnO has attracted a considerable amount of research interest as a prime candidate for nanoscale optoelectronics applications, including photodetectors, light emitting diodes, and lasers.³⁻¹⁰ Additionally, due to a large surface-to-volume ratio of the inherent nature of nanostructures, ZnO nanorods have been found to exhibit several intriguing phenomena, such as high sensitivity and fast response for the detection of gas molecules¹¹ and a novel behavior called photoelastic effect.¹² The photoelastic effect is defined as an external electromagnetic wave is capable of producing a change in the internal strain of a material.¹³ It is known that ZnO is a good piezoelectric material,^{1,14} in which an electric field can induce a strain, and

vice versa. Because oxygen defects have been well established to exist on the surface of ZnO,^{15,16} they have the ability to trap electrons, thereby creating a surface electric field. This process results in an upward band bending near the surface. Through the converse piezoelectric effect, ZnO nanorods will embody an internal stress. After photon excitation, the spatially separated photoexcited carriers can screen the built-in electric field, and changes the internal strain. Therefore, an incident light beam is able to induce a change in the internal strain, and it leads to the so-called photoelastic effect.¹³⁻¹⁵ In this paper, we further explore the characteristic of this novel property by studying its size dependence in ZnO nanorods. It is found that with decreasing diameter of ZnO nanorods, the magnitude of photoelastic effect increases. For example, the amounts of blue-shift in photoluminescence (PL) peak as well as low-frequency-shift in Raman spectra peak are larger when ZnO nanorods with a smaller diameter are exposed to a light beam. As a consequence, one can manipulate the photoelastic properties of ZnO nanorods via their diameters, a trait that is very useful for the application of optoelectric devices based on ZnO nanorods.

4.2 Experiment

ZnO nanorods were grown on *a*-plane sapphire substrates via the

vapour-liquid-solid (VLS) growth process.¹⁷ To manipulate the diameter of ZnO nanorods, we coated Au film with different thicknesses onto different areas of a piece of sapphire substrate. After VLS growth process, ZnO nanorods with a larger diameter will be grown on the area with a thick Au film. Scanning electron microscopy (SEM) images were recorded using a JEOL JSM 6500 system. Micro-photoluminescence (μ -PL) and micro-Raman (μ -Raman) scattering measurements were all performed at room temperature in a backscattering geometry using a Jobin Yvon T64000 system working in the triple-subtractive mode. The incident and scattered light propagated parallel to the *c*-axis, which in turn was normal to the growth surface. The sample was excited by a continuous wave (cw) He-Cd laser working at 325 nm, and a neutral density filter was used to control the laser intensity. In addition, a relaxed ZnO film with the *c*-plane facet grown on a sapphire substrate was used as a reference sample.¹⁸

4.3 Results and Discussion

As shown in Fig. 4.1, three different sizes of ZnO nanorods have been successfully grown. The ZnO nanorods form a well-organized hexagonal shape with diameters of (a) 250-300 nm, (b) 150-250 nm, and (c) 70-100 nm. In order to test the influence of size on the optical properties ZnO nanorods, we have performed μ -PL measurements as shown in Fig. 4.2. The sharp ultraviolet (UV) emission can be attributed to the

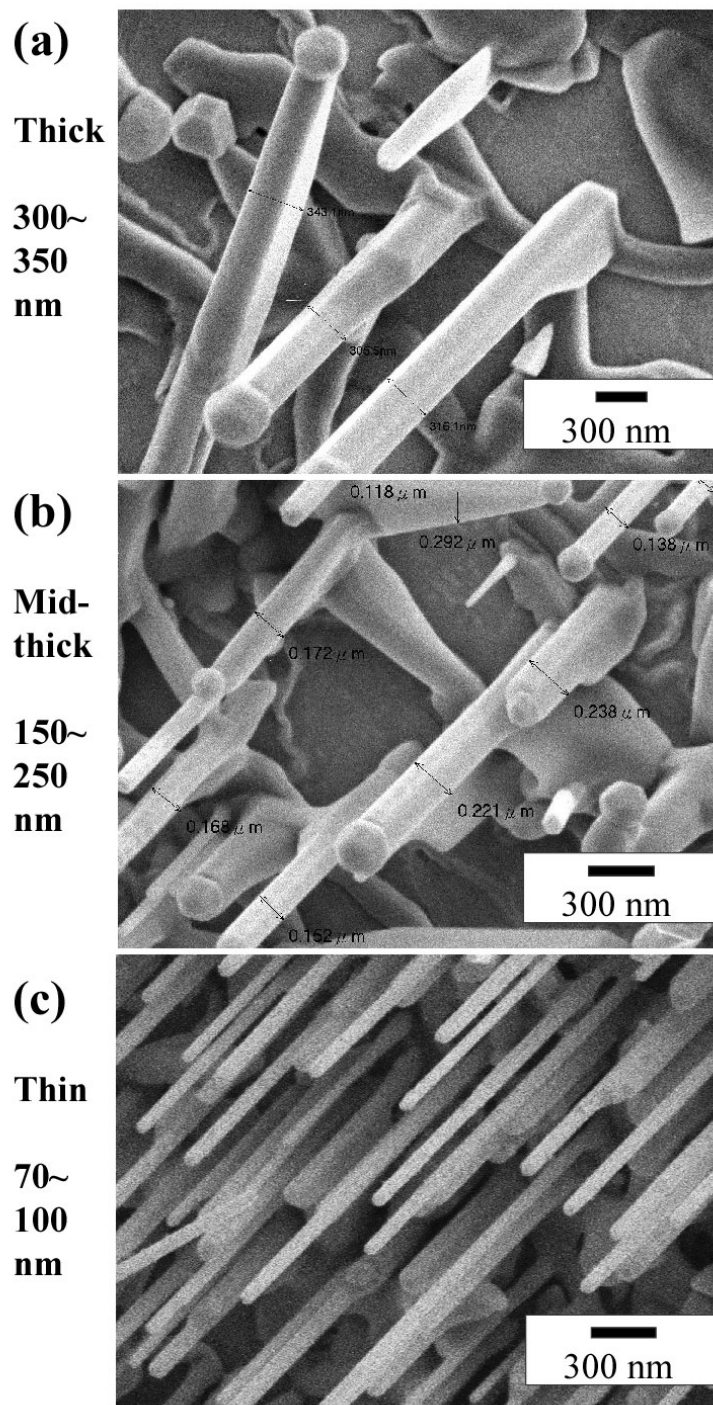


Fig. 4.1
Scanning electron microscopy images of ZnO nanorods
with different diameters.

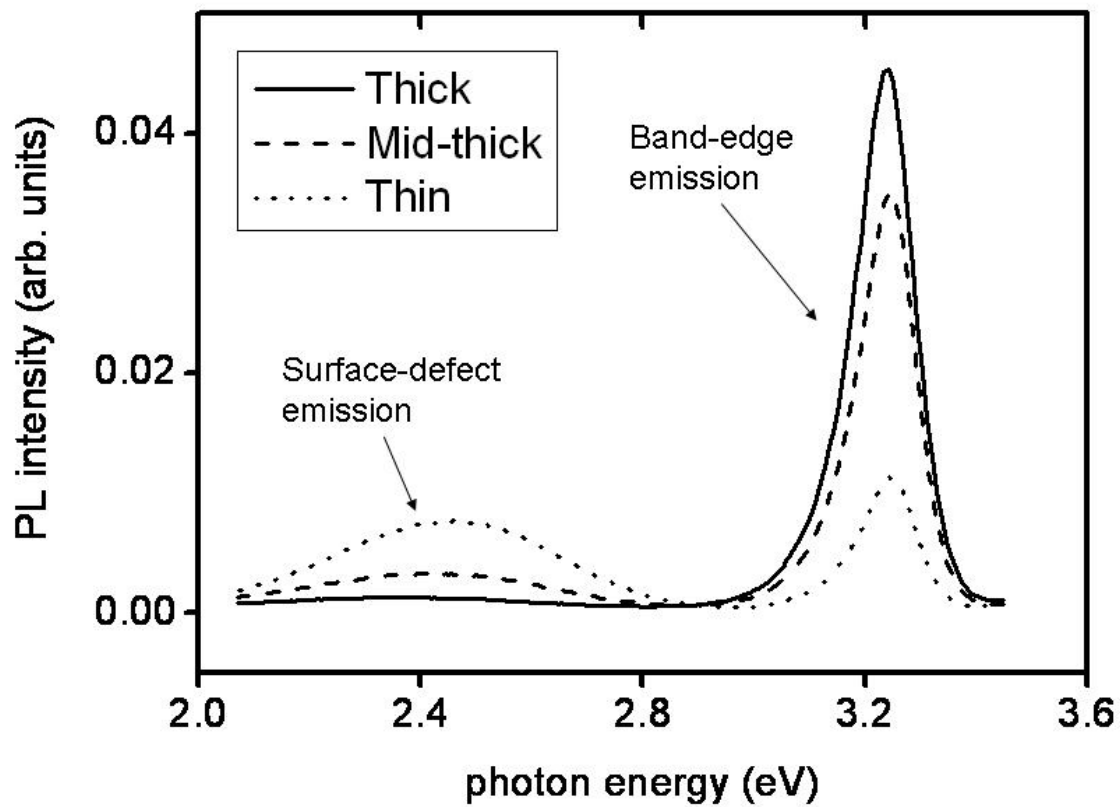


Fig. 4.2
Photoluminescence spectra of ZnO nanorods with different diameters.

band-edge transition, while the broad visible emission is due to the surface-defect-state transition.¹⁹ It is worth noting that with increasing diameter of ZnO nanorods, the surface-defect emission decreases while the band-edge emission enhances. The variation in intensities of band-edge emission and surface-defect emission can be attributed to the difference in the surface-to-volume ratio of nanorods with different diameters. More specifically, the relative intensity between the band-edge and surface-defect emission can be described by,¹⁹

$$\frac{I_{BE}}{I_{SD}} = C \left(\frac{r^2}{2rt - t^2} - 1 \right), \quad (4.1)$$

where I_{BE} and I_{SD} are the PL intensities of band-edge emission and surface-defect emission, respectively, r is the radius of nanorods, while C and t are constants which could be determined by experiments. As shown in Fig. 4.3, our experimental data can be well interpreted in terms of Eq. (4.1).

As shown in Figs. 4.4 and 4.5, we can clearly see that the peak position of the band-edge emission of ZnO nanorods shows a blue-shift with increasing excitation power density, while the A1(LO) phonon energy shows a low-frequency-shift in Raman scattering spectra. Note that the heating effect due to light illumination was not significant in our measurements, because it would otherwise result in a reduction in the PL peak energy. This phenomenon can be explained based on the underlying mechanism of the photoelastic effect as follows. Under optical excitation, the

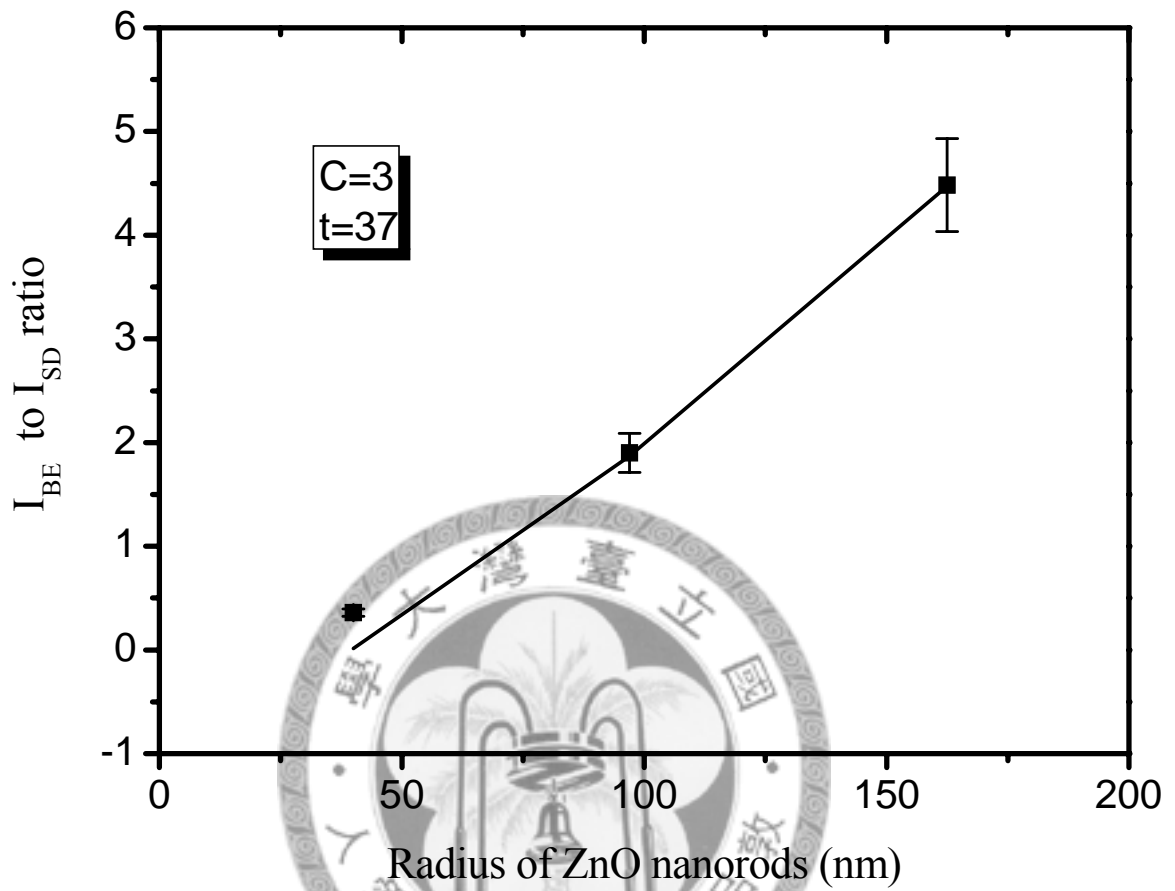


Fig. 4.3

Integrated intensity ratio between band-edge and defect emissions as a function of average wire radii, and a fit using Eq. (4.1)

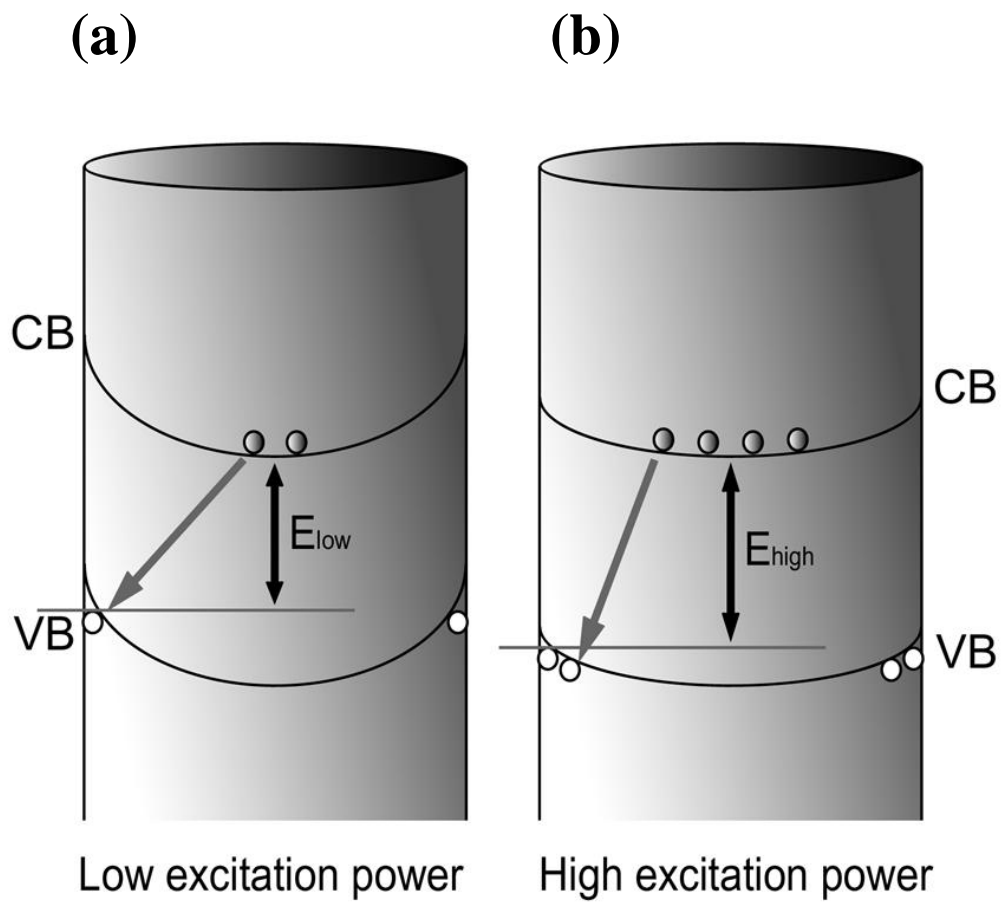


Fig. 4.4

Schematic of the band bending of ZnO nanorods under (a) low and (b) high optical excitation power.

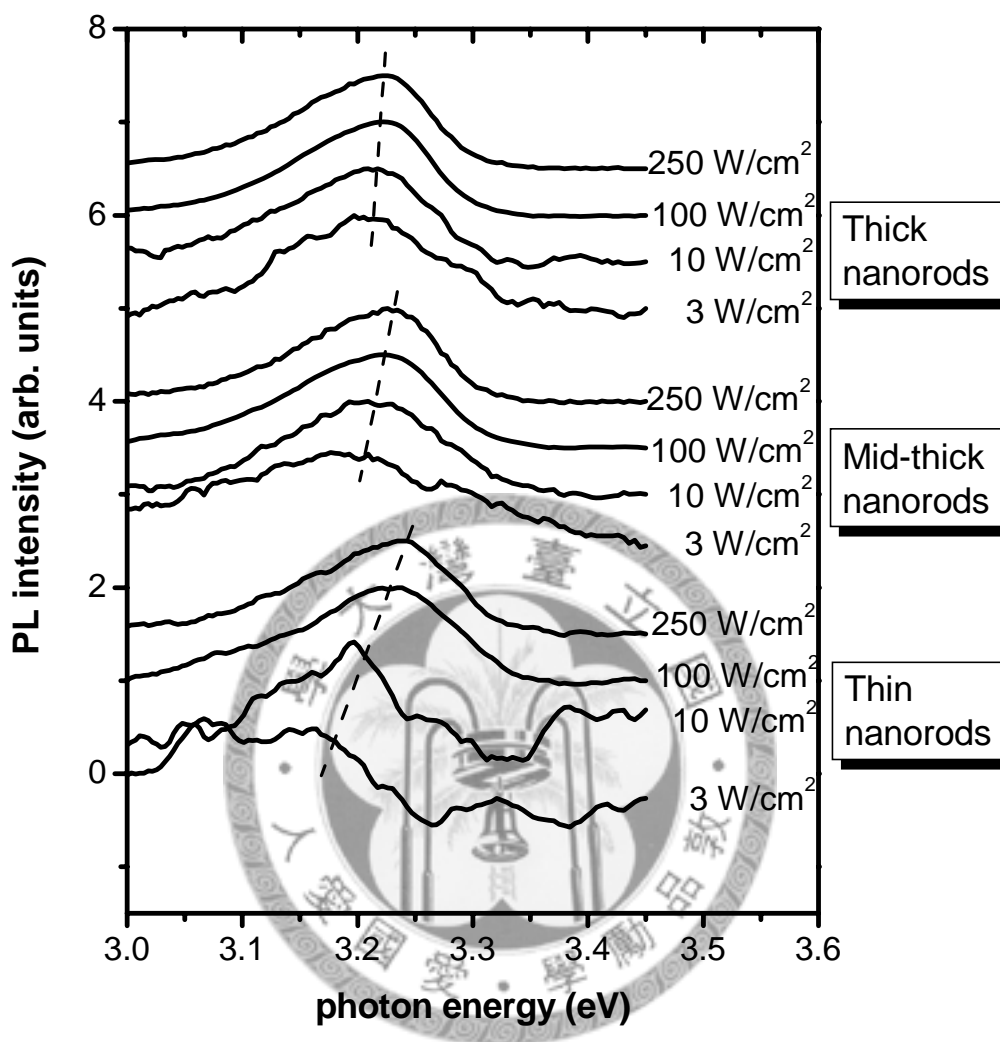


Fig. 4.5

Excitation-power-dependence of photoluminescence spectra for ZnO nanorods with different diameters. The excitation power increases from the bottom spectrum to top for each set.

photoexcited electrons and holes are swept in opposite directions by the built-in electric fields. The electrons accumulate at the center of the nanorods, while the holes get confined at the surface and neutralize the negatively charged states. Upon further increasing excitation power, more photoexcited holes can significantly neutralize the negatively charged states. The enhanced screening effect will decrease the built-in electric field and diminish the band bending near the surface, therefore, the transition energy gets higher as shown in Fig. 4.4. Besides, the screening of the built-in electric field by photoexcited electron-hole pairs will reduce the internal strain through piezoelectric effect. Therefore, the stressed ZnO lattice tends to be relaxed and the A₁(LO) phonon energy in Raman spectra is red-shifted as shown in Fig.4.5.

Since the photoelastic effect comes from the existence of defect states on the surface of ZnO nanorods, a larger photoelastic effect in thinner nanorods could be expected due to their larger surface to volume ratio. This prediction has been examined by the measurement of excitation-power-dependent μ -PL on ZnO nanorods with different diameters as shown in Fig. 4.5. It is clear that the peak position of band-edge emission shifts toward the high-energy side with increasing excitation power, and the amount of blue-shift in thinner rods is much more than that in thicker rods. This result confirms the inherent nature of the photoelastic effect that ZnO nanorods with a smaller diameter have a larger surface to volume ratio and will exhibit a larger photoelastic

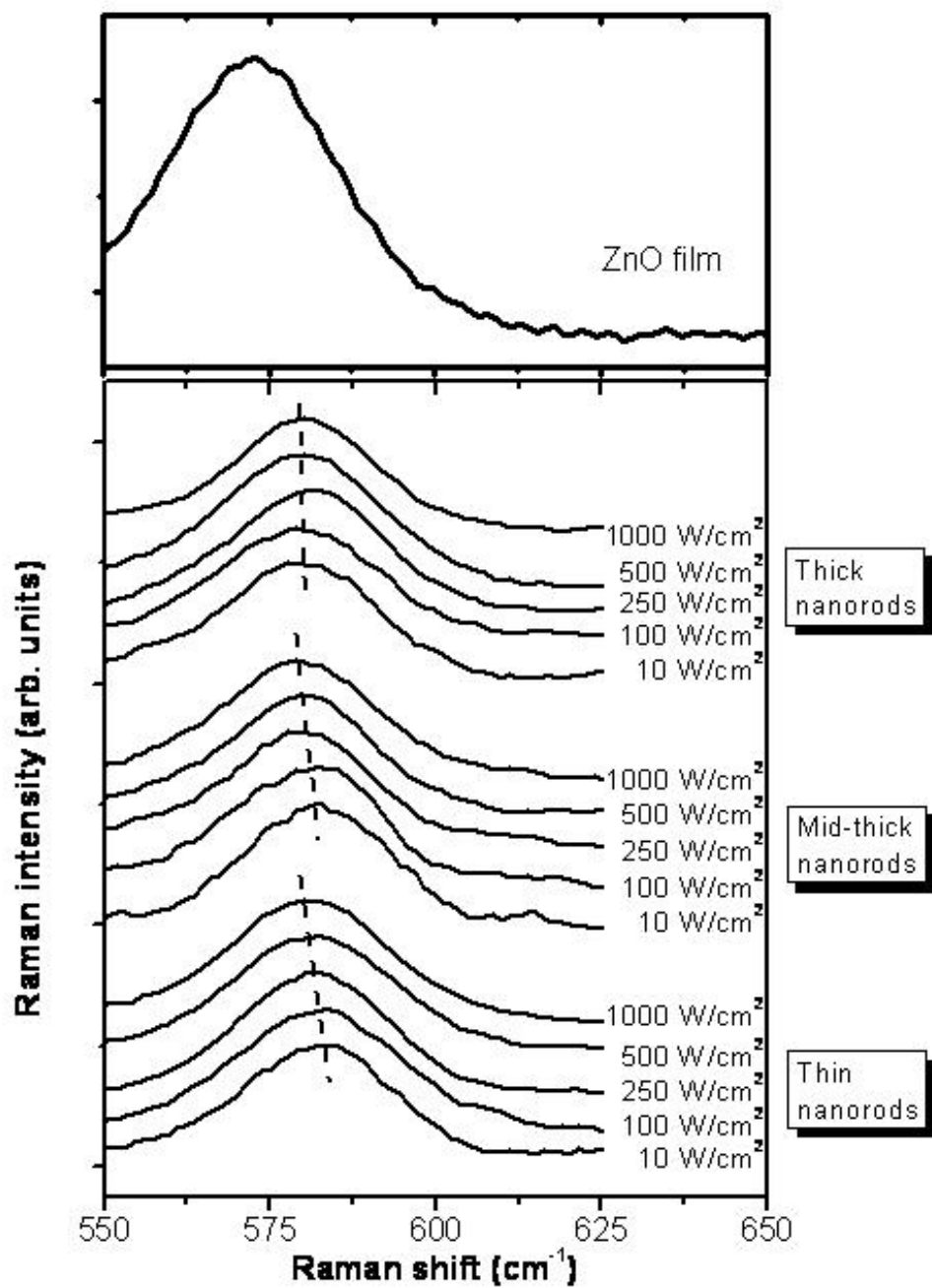


Fig. 4.6

Excitation-power-dependent Raman scattering spectra of ZnO film and ZnO nanorods with different diameters. The excitation power increases from the bottom spectrum to top for each set.

effect.

To further confirm our prediction, let us examine excitation-power-dependent Raman scattering spectra as shown in Fig. 4.6. According to previous studies, the frequency at ~580 nm can be assigned to A1 (LO) mode.²²⁻²² As described above, the internal strain arises from the built-in surface electric field through the converse piezoelectric effect. We can clearly see a low-frequency shift of A1(LO) peak mode in Raman scattering spectra due to the enhanced strain relaxation when the excitation intensity was increased. It is found that in thinner nanorods, the amount of peak shift is larger than that in thicker nanorods. As a consequence, this result further confirms the fact that the photoelastic effect does depend on the diameter of ZnO nanorods.

In order to have a more quantitative description of the Raman spectra, the magnitude of the strain in ZnO nanorods was estimated according to the induced phonon shift by the following expression²³:

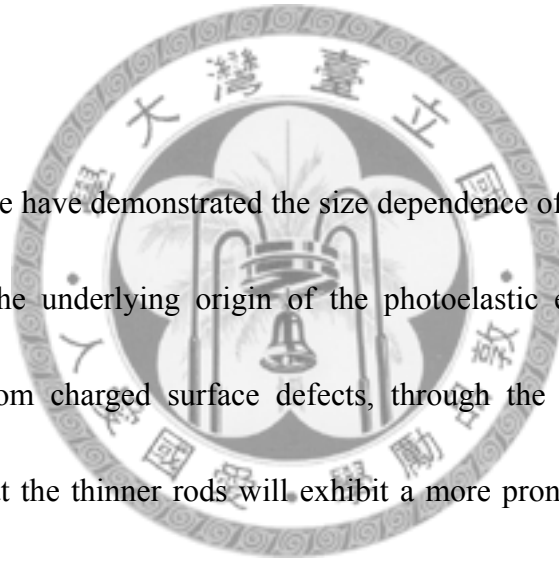
$$\varepsilon_{aa} \equiv (a - a_0)/a_0 = \frac{\Delta\omega}{2\left(a - b \frac{C_{13}}{C_{33}}\right)}, \quad (4.2)$$

where $\Delta\omega$ is the deviation in frequency of the A1 (LO) phonon, a and a_0 are respectively the strained and unstrained lattice constants of ZnO crystals, a_λ and b_λ are the phonon deformation potential parameters, C_{13} and C_{33} are the elastic constants, and ε_{aa} is the biaxial strain in the c-plane. The frequency shift $\Delta\omega$ of ZnO nanorods (relative to the relaxed ZnO film) was obtained by the Raman scattering spectra as shown in Fig. 4.6,

and the parameters $C_{13} = 90$ GPa, $C_{33} = 196$ GPa, $a_{\lambda} = -690$ cm^{-1} , and $b_{\lambda} = -940$ cm^{-1} were taken from previous reports^{24,25}. Figure 4.7 shows the A1 (LO) mode frequency and the biaxial strain (ϵ_{aa}) in our measured samples as a function of the excitation power. Clearly, the compressive biaxial strain in c-plane of nanorods decreases with increasing excitation power; moreover, we can clearly see that the thinner ZnO nanorods exhibit a larger relaxation of biaxial strain.

4.4 Conclusion

In conclusion, we have demonstrated the size dependence of the photoelastic effect in ZnO nanorods. The underlying origin of the photoelastic effect has been firmly confirmed arising from charged surface defects, through the converse piezoelectric effect. It is found that the thinner rods will exhibit a more pronounced effect due to a larger surface to volume ratio. Our study shown here can be extended to many other nanoscaled materials. The research along the guideline shown here should be very useful for the application of nanoscaled semiconductors in optical modulators.



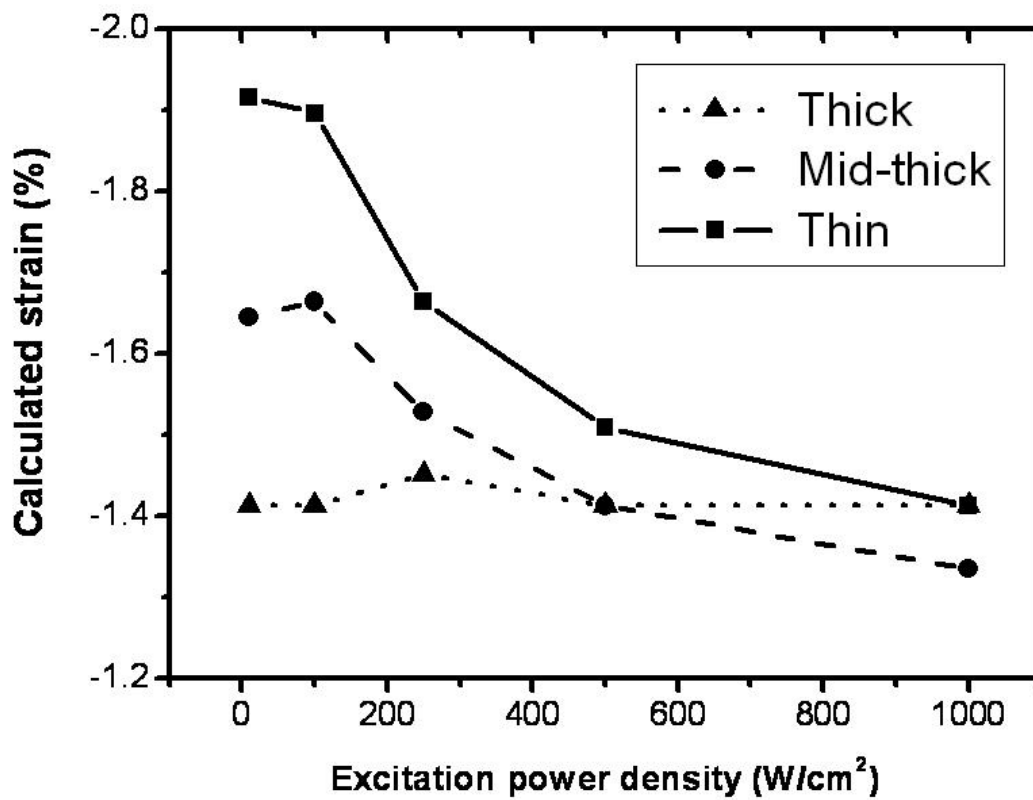


Fig. 4.7

The estimated strength of the biaxial strain as a function of the excitation power for ZnO nanorods for different diameters.

Reference

1. Ozgur U , Alivov Ya I, Liu C, Teke A, Reshchikov M A, Dogan S, Avrutin V, Cho S-J and Morkoc H (2005), J. Appl. Phys. **98** 041301.
2. White H and Ryu Y (2006), Compound Semicond. **12** 16.
3. P. M. Petroff, A. C. Gossard, and W. Wiegmann (1984), Appl. Phys. Lett. **45**, 620.
4. D. Gershoni, H. Temkin, D. J. Dolan, J. Dunsmuir, S. N. G. Chu, and M. B. Panish (1988), Appl. Phys. Lett. **53**, 995.
5. M. Yazawa, M. Koguchi, and K. Hiruma (1991), Appl. Phys. Lett. **58**, 1080.
6. C. M. Lieber (2001), Sci. Am. **285** (3), 58.
7. M. H. Huang, S. Mao, H. Feick, H. Yan, Y. Wu, H. Kind, E. Weber, R. Russo, and P. Yang (2001). Science **292**, 1897.
8. Kind H, Yan H, Messer B, Law M and Yang P (2002), Adv. Mater. **14** 158.
9. Liu C, Zapien J A, Yao Y, Meng X, Lee C S, Fan S S, Lifshitz Y and Lee S T (2003), Adv. Mater. **15** 838.
10. Yang P, Yan H, Mao S, Russo R, Johnson J, Saykally R, Morris N, Pham J, He R and Choi H-J (2002), Adv. Funct. Mater. **12** 323.
11. Wan Q, Li Q H, Chen Y J, Wang T H, He X L, Li J P and Lin C L (2004), Appl. Phys. Lett. **84** 3654.
12. T T Chen, C L Cheng, S-P Fu and Y F Chen (2007), Nanotechnology **18** 225705.

13. Nye J F 1972 *Physical Properties of Crystals* (London: Oxford University Press).
14. Dal Corso A, Posternak M, Resta R and Baldereschi A (1994), *Phys. Rev. B* **50** 10715.
15. Vanheusden K, Warren W L, Seager C H, Tallant D R, Voigt J A and Gnade B E (1996), *J. Appl. Phys.* **79** 7983.
16. Li Q H, Gao T, Wang Y G and Wang T H (2005), *Appl. Phys. Lett.* **86** 123117.
17. Lin J M, Lin H Y, Cheng C L and Chen Y F (2006), *Nanotechnology* **17** 4391.
18. Lin M-Z, Su C-T, Yan H-C and Chern M-Y (2005), *Japan. J. Appl. Phys.* **44** L995.
19. Ilan Shalish, Henryk Temkin, and Venkatesh Narayanamurti (2004), *PHYSICAL REVIEW B* **69**, 245401.
20. Hayes W and Loudon R (1978), *Scattering of Light in Crystals* (New York: Wiley).
21. Zhang Y, Jia H, Wang R, Chen C, Luo X, Yu D and Lee C (2003), *Appl. Phys. Lett.* **83** 4631.
22. Calleja J M and Cardona M (1977), *Phys. Rev. B* **16** 3753.
23. Wagner J-M and Bechstedt F (2000), *Appl. Phys. Lett.* **77** 346.
24. Azuhata T et al (2003), *J. Appl. Phys.* **94** 968.
25. Gruber Th, Prinz G M, Kirchner C, Kling R, Reuss F, Limmer W and Waag A (2004), *J. Appl. Phys.* **96** 289.

Chapter 5

Summary



Chapter 5 Summary

In summary, optical properties of two nanostructures of semiconductor, InGaN/GaN multiple quantum wells (MQWs) and ZnO nanorods, were investigated in this thesis.

We first demonstrated the detection of DNA hybridization with the build-in piezoelectric (PZ) field and quantum confined Stark effect in InGaN/GaN MQWs. A 5-nm-Au layer was sputtered on the MQWs structure, and then single-stranded DNA molecules with thiol modified were immobilized on the Au surface as probes. As the sample was exposed to matched target DNA solution, the peak position of PL spectra shifts toward the high-energy side, while the A₁(LO) mode of Raman spectra shifts toward the low-energy side due to the change in PZ field and QCSE from DNA hybridization. However, the PL and Raman spectra reveal no shift in the mismatched DNA solution because the hybridization process does not occur. The result could provide a useful contribution for DNA-sequence identification and development of biochips.

Latter, size-dependent photoelastic effect in ZnO nanorods was studied based on their surface defect states and PZ effect. Three different diameters of ZnO nanorods were grown on the c-plane of sapphire substrate by vapour-liquid-solid deposition

method. In this work, it was observed that a novel phenomenon called photoelastic effect exists in ZnO nanorods, especially in thin nanorods. For our sample, with increasing excitation power, the PL peak of band-gap emission shifts toward the high-energy side, while the A₁(LO) mode of Raman spectra shifts toward the low-energy side due to the band bending effect from surface defects and the screening effect by the photoexcited carriers. The above phenomenon shows more pronounced in thinner nanorods due to their larger surface to volume ratio, which leads more serious band-bending effect near the surface of the nanorods, such that there exists greater photoelastic effect in thinner ones. Our results should be very useful for the application of ZnO based nanoscale optoelectronic devices, and they can also be extended to the study of other nanostructured semiconductors.

